Tightly Coupled Ultrashort Baseline and Inertial Navigation System for Underwater Vehicles: An Experimental Validation

M. Morgado
Department of Electrical and Computer Engineering, Instituto Superior Técnico, Universidade Técnica de Lisboa, Lisbon, Portugal
e-mail: marcomorgado@isr.ist.utl.pt
P. Oliveira
Department of Mechanical Engineering, Instituto Superior Técnico, Universidade Técnica de Lisboa, Lisbon, Portugal
e-mail: pjcro@isr.ist.utl.pt
C. Silvestre
Department of Electrical and Computer Engineering, Instituto Superior Técnico, Universidade Técnica de Lisboa, Lisbon, Portugal
Department of Electrical and Computer Engineering, Faculty of Science and Technology, University of Macau, Taipa, Macau, China
e-mail: cjs@isr.ist.utl.pt

Received 14 November 2011; accepted 4 October 2012

This paper presents a new ultrashort baseline (USBL) tightly coupled integration technique to enhance error estimation in low-cost strapdown inertial navigation systems (INSs), with application to underwater vehicles. In the proposed strategy, the acoustic array spatial information is directly exploited in an extended Kalman filter (EKF) implemented in a direct feedback structure. Instead of using the USBL position fixes or computed range and elevation/bearing angles to correct the INS error drifts, as in classical loosely coupled strategies, the novel tightly coupled strategy directly embeds in the EKF the round-trip-time and time-difference-of-arrival of the acoustic signals arriving at the onboard receivers. The enhanced performance of the proposed filtering technique is evidenced both through extensive numerical simulations and with experimental data obtained in field tests at sea. The tightly coupled filter is also shown to be able to operate closer to theoretical performance lower bounds, such as the posterior Cramér-Rao lower bound, using Monte-Carlo simulations. This paper details the design and description of an USBL/INS prototype to be used as a low-cost navigation system, including the acoustic processing and positioning system, fully developed in-house. The developed system validates the usage of the proposed technique with real data in real world operation scenarios, and its enhanced performance compared to classical strategies is evaluated experimentally (median improvement level of 15% in typical operating conditions). Improved and faster convergence to nominal trajectories from multiple initial conditions, as well as enhanced accelerometer and rate gyros estimation capabilities, are also demonstrated experimentally for the new tightly coupled filter.

1. INTRODUCTION

Worldwide, there has been an increasing interest in the use of underwater vehicles to expand the ability to accurately survey large ocean areas. Routine operations such as environmental monitoring, surveillance, underwater inspection of estuaries, harbors and pipelines, and geological and biological surveys—see Pascoal et al. (2000)—are tasks commonly performed at present either by remotely operated vehicles (ROVs) or by autonomous underwater vehicles (AUVs). The use of these robotic platforms requires low-cost, compact, high-performance, robust navigation systems that can accurately estimate the vehicle's position and attitude. In fact, the design and implementation of navigation systems stands out as one of the most critical steps toward the successful operation of autonomous vehicles and marine robotic vehicles. The ability to perform the aforementioned procedures at increasing depths, often life-threatening or impossible for humans, makes marine robotic vehicles stand out as one of the strongest areas of investigation and efforts by the robotics scientific community (Bowen et al., 2009; Jalving et al., 2003; Lurton and Millard, 1994; Napolitano et al., 2005). For other interesting and detailed surveys on underwater vehicle navigation and its relevance, see Whitcomb (2000) and more recently Kinsey et al. (2006). This paper presents a new tightly coupled integration technique to enhance error estimation in strapdown inertial navigation systems (INSs) for underwater vehicles, in which the acoustic array spatial information is directly exploited in the navigation system algorithm, while

Direct correspondence to: M. Morgado, e-mail: marcomorgado@isr.ist.utl.pt

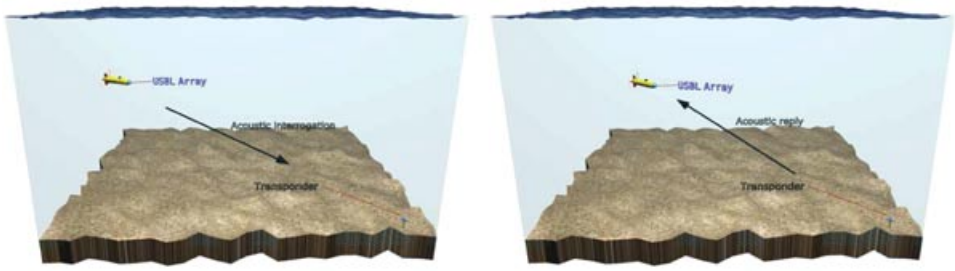

(a) The vehicle interrogates the transponder with an acoustic signal (b) The transponder replies after detection of the inbound acoustic signal

Figure 1. Typical mission scenario—an underwater vehicle, equipped with an INS and an inverted USBL array, interrogates a nearby transponder and listens for its acoustic responses to obtain transponder relative position measurements.

focusing on low-cost and affordable high-performance navigation platforms.

INSs provide a self-contained passive means for three-dimensional positioning in the open ocean with excellent short-term accuracy. However, unbounded positioning errors induced by the uncompensated rate gyro and accelerometer errors degrade INS accuracy over time. This performance degradation and the limitations inherent in low-cost INSs, attributed to open-loop unbounded estimation errors, uncompensated sensor noise, and bias effects, are often tackled by merging additional information sources with nonlinear filtering techniques. Among a diverse set of techniques (Bar-Shalom et al., 2001; Crassidis, 2006), an extended Kalman filter (EKF) in a direct-feedback configuration (Brown and Hwang, 1997; Vasconcelos et al., 2011) is commonly adopted to estimate and compensate for the accumulation of the INS integration errors. Within the multitude of available aiding devices, such as inclinometers, magnetic compasses, Doppler velocity loggers (DVLs), depth pressure sensors, laser range finders, etc., the global positioning system (GPS) is a very popular choice and a commonly adopted solution in aerial and land-based applications (Grewal et al., 2007; Sukkarieh et al., 1999). The opacity (i.e., high attenuation) of the ocean environment to most electromagnetic signals makes acoustic propagation the preferable method to obtain practical range measurements. Other practical navigation methodologies that do not use acoustics typically involve surfacing the vehicle regularly to obtain intermittent GPS corrections (Yun et al., 1999). Available underwater acoustic positioning systems (Milne, 1983; Vickery, 1998)—such as long baseline (LBL) systems, which entail cumbersome and time-consuming installation and calibration procedures; hull-mounted short baseline (SBL) systems, which have to be rigidly mounted to a vessel hull and are affected by the natural bending of the hull; and finally ultrashort baseline (USBL) systems, which provide factory-calibrated and fast deployable systems that are suited for low-cost navigation systems—stand often as the primary choice for underwater positioning (Jaffré et al., 2005; Kinsey and Whitcomb, 2004; Lee et al., 2004; Miller et al., 2010; Smith and Kronen, 1997).

This paper addresses the synthesis and design of modern navigation systems with application to underwater vehicles, focusing on small arrays of acoustic receivers as the main sensor suite installed onboard the underwater vehicle, in particular with what is known as an USBL acoustic positioning system (Milne, 1983). The considered mission scenarios are illustrated in Figure 1, which displays an underwater vehicle that is equipped with an INS and an USBL array in an inverted USBL configuration (Vickery, 1998) that interrogates a single nearby transponder located in a known position of the vehicle's mission area, engaging in interrogations over considerable distances ranging typically from a few meters to several kilometers. This interrogation scheme to obtain the round-trip-time (RTT) of travel of the acoustic waves allows for the use of low-cost clocks onboard the vehicle to obtain driftless range measurements. Recent advances in underwater navigation relying on synchronous one-way travel times of acoustic waves, available from costly higher precision oscillators, were presented by Eustice et al. (2011). In addition to paving the way for future fully autonomous systems that do not require surface mission support vessels, inverted USBL configurations allow for the sound velocity to be considered constant while operating in the same underwater layer as the transponders (for instance, bottom operation while interrogating a bottom placed transponder). These kinds of inverted configurations also allow for other underwater autonomous routine operations, such as underwater interventions as well as homing and docking to underwater stations (Jaffré et al., 2005; Sanz et al., 2010). An overview of USBL/INS tightly coupled technology entry points into underwater navigation is presented in Figure 2, where the solution presented herein is built upon state-of-the-art inverted USBL loosely coupled solutions and introduces enhanced performance through full tightly coupled INS/USBL configurations. The claimed performance enhancement of the novel tightly coupled solution is demonstrated in comparison with the state-of-the-art loosely coupled USBL, which also estimates the INS inertial sensors biases, whereas classical and substandard solutions are not considered.

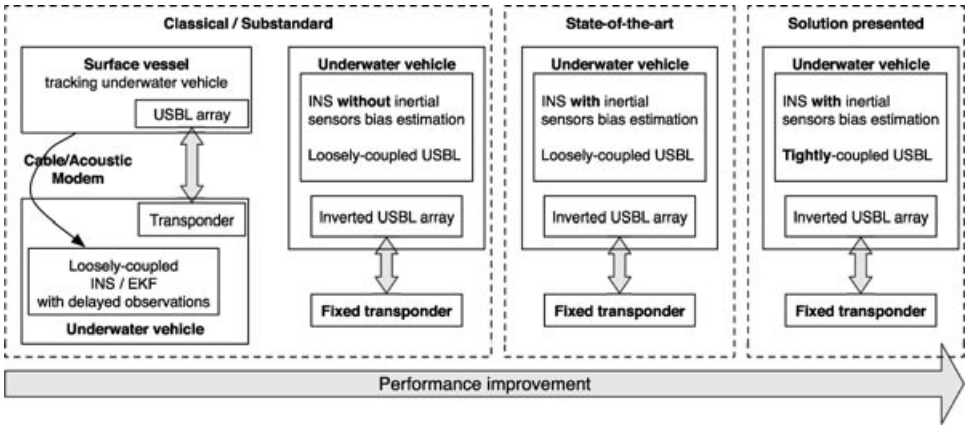

Figure 2. Overview of coupling technologies on USBL/INS sensor fusion—classical structures, in which the USBL array tracks underwater vehicles while mounted on surface vessels, need to relay the positioning information through cables or acoustic modems. Classical and substandard INS solutions typically do not estimate the inertial sensor biases resulting in very poor performance, while state-of-the-art technology offers improved navigation capabilities by moving the USBL array onboard the underwater vehicle (inverted USBL) and estimating rate gyros and accelerometer biases. The solution presented herein builds upon state-of-the-art inverted USBL loosely coupled solutions and introduces enhanced performance through full tightly coupled USBL and INS configurations.

1.1. Motivation

Typical USBL/INS integration techniques, usually referred to as loosely coupled (Grewal et al., 2007), rely on solving positioning and sensor fusion problems separately, not taking into account the acoustic array geometry in the navigation system. The new proposed tightly coupled USBL/INS integration strategy directly exploits the acoustic array spatial information, resorting to an EKF in a direct-feedback configuration. A loosely coupled system is commonly known in the literature (Grewal et al., 2007) as a modular system in which each module is able to operate on its own and can be easily decoupled from the others.

A typical example of a loosely coupled system is a GPS positioning device providing world coordinate position fixes, whereas an INS provides open-loop integration of the inertial sensors, and the information fusion is performed *a posteriori*. In this framework, the INS does not have any prior knowledge on what kind of position fix algorithm is being applied to the pseudoranges measured to each orbiting satellite, nor is the GPS aware of to which entity it is providing information. In a tightly coupled configuration, both entities are aware of each other's existence and cooperate, in some sense, to provide enhanced performance to the end-user. In a tightly coupled system, the GPS system directly provides the measured satellite pseudo ranges to the INS algorithm, whereas the INS algorithm estimates, among other inertial system errors, the user clock bias and drift, propagation delays, errors derived from atmospheric effects, and other associated GPS errors (Grewal et al., 2007). Tightly coupled approaches for the GPS/INS navigation problem for aerial and land vehicles have been addressed previously in the literature (Knight, 1997; Yi and Grejner-Brzezinska, 2006). Nevertheless, to the best of our knowledge, this paper and the work presented herein represents the first time that a tightly coupled strategy has been applied to underwater navigation using small arrays of acoustic receivers such as an USBL positioning system.

1.2. Paper Organization

The paper is organized as follows: The core USBL acoustic positioning sensor is first described in Section 2, and the main aspects of the navigation system and the proposed architecture are presented in Section 3. The EKF-based inertial error model is introduced in Section 3.1, and both the new tightly coupled and classical loosely coupled integration strategies are detailed in Section 3.2 while implementation and discretization details are briefly outlined in Section 3.3. Section 4 provides an analysis based on numerical simulation results and a comparison to theoretical performance lower bounds, namely the posterior Cramér-Rao lower bound (PCRLB). The prototype system design is presented in Section 5 and the experimental evaluation and validation of the proposed technique is reported in Section 6. Finally, Section 7 presents some concluding remarks and comments on future directions of research.

2. ULTRASHORT BASELINE POSITIONING SYSTEM

This section introduces the main sensor suite adopted in this work. The USBL sensor consists of a small and compact array of acoustic transducers that allows for the

computation of a transponder position in the vehicle coordinate frame, based on the travel time of acoustic signals emitted by the transponder (Milne, 1983). This travel time is obtained from the RTT of travel of acoustic signals from the pinger installed on the vehicle to the transponder placed at a known position and back to the receivers on the USBL array. Taking into account the quantization performed by the acoustic system, and assuming that the transponder performs a similar acoustic processing, the RTT to each of the receivers on the USBL array is given by

$$t_{\mathrm{RTT}\,i} = [\bar{t}_p + \varepsilon_t]_{T_s} + \bar{t}_d + [\bar{t}_{r\,i} + \varepsilon_c + \varepsilon_{d\,i}]_{T_s},$$

where $\bar{t}_p$ is the nominal travel time from the pinger on the vehicle to the transponder, $\bar{t}_{r\,i}$ is the nominal travel time from the transponder to the ith acoustic receiver, $[\cdot]_{T_s}$ represents the acoustic sampling quantization

$$[x]_{T_s} = T_s \,\mathrm{round}(x/T_s), \quad x \in \mathbb{R},$$

where T_s is the acoustic sampling period (and consequently the maximal available time-resolution), and round$(\cdot)$ is the standard mathematical *round-to-nearest-integer* operator. The terms ε_t and ε_c represent, respectively, the noise at the transponder and at the receivers (common to all receivers—it includes transponder-receiver relative motion time-scaling effects and errors in sound propagation velocity), and $\varepsilon_{d\,i}$ captures additional differential error sources, much smaller than the common mode errors. The response delay time $\bar{t}_d$ is considered to be known, so it can be removed upon reception of the signals.

The measurements of transponder-receivers travel times are commonly obtained by dividing the RTT by 2, as suggested in Milne (1983). It is then reasonable to consider, under the vehicle stationary assumption during the interrogation/reply cycle (valid for short interrogation distances and slow vehicle speed such as those considered in this work) and neglecting the small time difference induced by the position of the onboard acoustic trigger/pinger relative to the receiving array, that the travel times between the transponder and the receivers can be computed by removing the known reply delay on the transponder and half of the average measured RTT,

$$t_{r\,i} = t_{\mathrm{RTT}\,i} - \bar{t}_D - \langle \mathbf{t}_{\mathrm{RTT}} \rangle / 2,$$

where $\langle \mathbf{t}_{\mathrm{RTT}} \rangle$ is the average of the RTT given by $\langle \mathbf{t}_{\mathrm{RTT}} \rangle = \sum_{i=1}^{n_r} t_{\mathrm{RTT}\,i}$. Thus, for the sake of simplicity, the range measurements between the transponder and the receivers installed onboard the vehicle (as measured by the USBL device) ρ_i are assumed to be

$$\rho_{i\,r} = v_p t_{r\,i} + \eta_c + \eta_{d\,i},$$

where v_p is the underwater sound speed, assumed to be known and constant for confined mission scenarios, η_c represents the measurement noise induced by the common error to all receivers, and the term $\eta_{d\,i}$ represents the differential noise induced by the additional error sources and the acoustic quantization performed by the USBL system. As depicted in Figure 3, the position of the transponder in the vehicle coordinate frame is given by

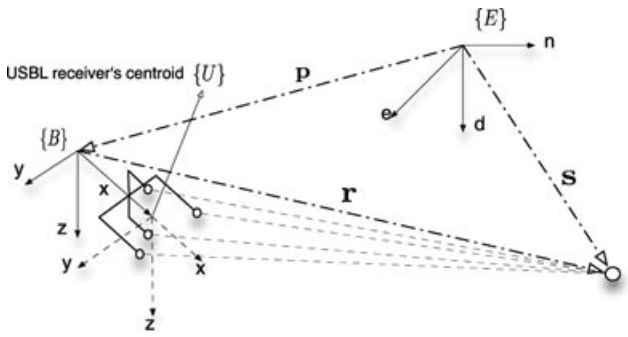

Figure 3. USBL system reference frames—the body-fixed coordinate frame is rigidly attached to the vehicle, while the Earth-fixed reference frame is attached to a fixed point on the mission area. The centroid of the onboard receivers serves as the reference point for the USBL reference frame. The north, east, and down axes in the Earth-fixed reference frame $\{E\}$ are represented, respectively, by the letters **n**, **e**, and **d**.

$$\mathbf{r} = \mathcal{R}^T(\mathbf{s} - \mathbf{p}), \tag{1}$$

where the matrix $\mathcal{R} \in SO(3)$ is the shorthand notation for the body $\{B\}$ to Earth $\{E\}$ coordinate frames rotation matrix ${}^E_B\mathbf{R}$, the operator $(\cdot)^T$ represents the matrix transpose [thus $\mathcal{R}^T \in SO(3)$ represents the inverse rotation matrix from $\{E\}$ to $\{B\}$], $\mathbf{r} \in \mathbb{R}^3$ is the position of the transponder in $\{B\}$, $\mathbf{s} \in \mathbb{R}^3$ is the position of the transponder in Earth-fixed coordinates, and $\mathbf{p} \in \mathbb{R}^3$ is the position of the vehicle in Earth-fixed coordinates. Let $\{U\}$ denote the coordinate frame attached to the USBL receiving array, which is centered at the centroid of the receivers such that

$$\sum_{i=1}^{n_r} {}^U\mathbf{b}_i = \mathbf{0},$$

where ${}^U\mathbf{b}_i \in \mathbb{R}^3$ denotes the position of the receiver in the USBL coordinate frame $\{U\}$, and n_r is the number of installed receivers on the array. The distances between the transponder and the receivers installed onboard the vehicle (as measured by the USBL device) can be written as

$$\rho_i = \|{}^U\mathbf{b}_i - {}^U\mathbf{r}\|, \tag{2}$$

where ${}^U\mathbf{r} \in \mathbb{R}^3$ is the position of the transponder in $\{U\}$. The installation of the USBL array on the vehicle can be described by a transformation defined in the special Euclidean group $SE(3)$ that relates vectors in $\{U\}$ to vectors in $\{B\}$. Let ${}^U\mathbf{x}$ be a vector in $\{U\}$, ${}^B_U\mathbf{R}$ be the installation rotation matrix between $\{U\}$ and $\{B\}$, and ${}^B\mathbf{p}_U$ be the installation position offset between $\{U\}$ and $\{B\}$. The representation of ${}^U\mathbf{x}$ in $\{B\}$ is given by

$${}^B\mathbf{x} = {}^B\mathbf{p}_U + {}^B_U\mathbf{R}\,{}^U\mathbf{x},$$

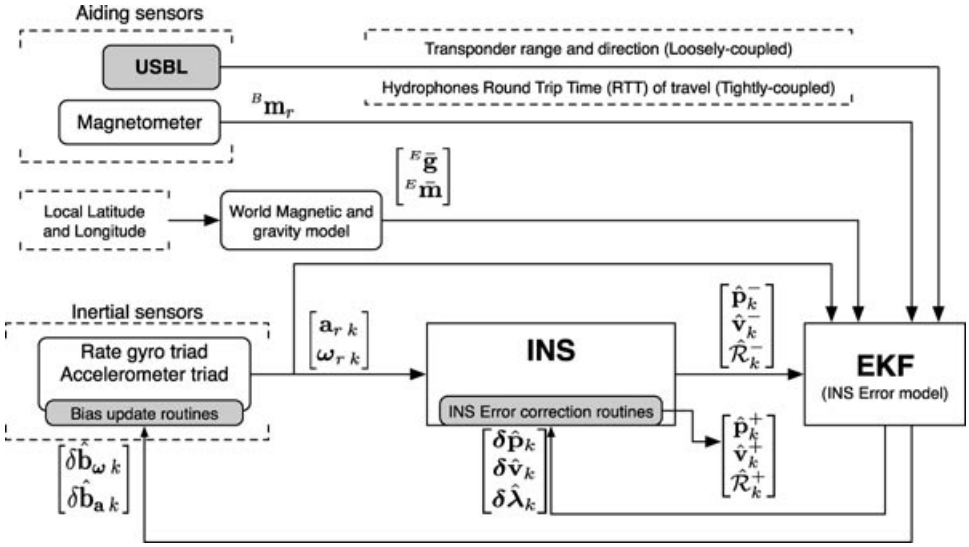

Figure 4. Navigation system block diagram—a direct-feedback loop in which an EKF dynamically estimates the INS errors and inertial sensors biases, with the aid of external sensors. The work presented in this paper focuses mostly on the measurement residual computation block and on the EKF observation models, to provide software-based improvements from the additional TDOA information, available from the tightly coupled USBL positioning system.

which allows us to write

$$^{U}\mathbf{x} = {}^{B}_{U}\mathbf{R}^{T}({}^{B}\mathbf{x} - {}^{B}\mathbf{p}_{U}). \tag{3}$$

Applying the frame transformation from Eq. (3), the distances between the transponder and the receivers in Eq. (2) can be simply written in the $\{B\}$ reference frame as

$$\begin{aligned}\rho_i &= \left\| {}^{B}_{U}\mathbf{R}^{T}(\mathbf{b}_i - {}^{B}\mathbf{p}_{U}) - {}^{B}_{U}\mathbf{R}^{T}(\mathbf{r} - {}^{B}\mathbf{p}_{U}) \right\| \\ &= \left\| {}^{B}_{U}\mathbf{R}^{T}(\mathbf{b}_i - \mathbf{r}) \right\| = \|\mathbf{b}_i - \mathbf{r}\|, \end{aligned} \tag{4}$$

where $\mathbf{b}_i \in \mathbb{R}^3$ denotes the position of the receiver in $\{B\}$. Finally, using Eq. (1) in Eq. (4) yields

$$\rho_i = \|\mathbf{s} - \mathbf{p} - \mathcal{R}\mathbf{b}_i\|. \tag{5}$$

3. USBL-AIDED INERTIAL NAVIGATION SYSTEM

This section details the USBL-aided inertial navigation architecture adopted in this work and presents the novel tightly coupled USBL sensor fusion technique in Section 3.2.2. The specific USBL sensor-based INS-aiding techniques are presented in Section 3.2, and implementation details are provided in Section 3.3. The overall architecture is briefly outlined here before introducing the EKF modeled inertial error dynamics in Section 3.1. Appendix D provides additional details on the internal structure of the INS algorithm used herein.

The INS is the backbone algorithm that performs attitude, velocity, and position numerical integration from rate gyro and accelerometer triads data, rigidly mounted on the vehicle structure (strap-down configuration). The nonideal inertial sensor effects, due to noise and bias, are dynamically compensated by the EKF to enhance the navigation system's performance and robustness. Position, velocity, attitude, and bias compensation errors are estimated by introducing the aiding sensors data in the EKF, and are thus compensated in the INS according to the direct-feedback (Brown and Hwang, 1997) configuration shown in Figure 4. The INS numerical integration algorithms adopted in this work are based on the work detailed in Savage (1998a) and Savage (1998b). Applications within the scope of this work are characterized by confined mission scenarios and limited operational time, allowing for a simplification of the frame set to Earth and body frames and the use of an invariant gravity model without loss of precision.

3.1. EKF Modeled Inertial Error Dynamics

In a stand-alone INS, bias and inertial sensor error compensation is usually performed based on extensive offline calibration procedures and data. The usage of filtering techniques in navigation systems allows for the dynamic estimation of inertial sensor nonidealities, bounding the INS errors. From the myriad of existing filtering techniques, such as particle filters and the unscented Kalman filter (UKF), among others, the EKF is used in this work to estimate and compensate for the INS errors. The inertial error dynamics, based on perturbational rigid body kinematics, were brought to full detail by Britting (1971) and are applied to local navigation by modeling the position, velocity, attitude, and bias compensation errors dynamics,

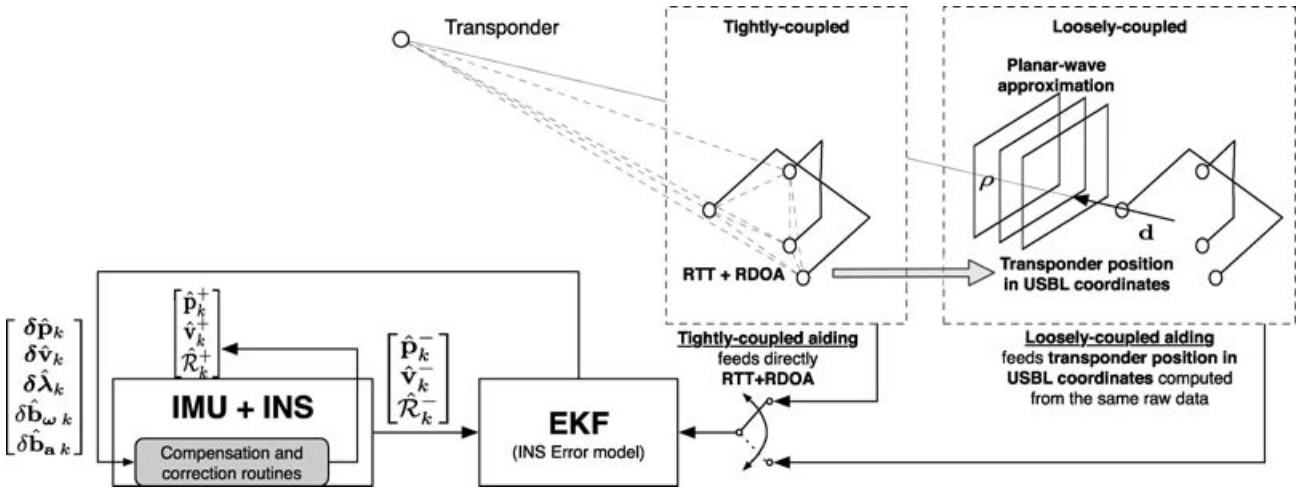

Figure 5. Overview of the sensor information being provided by the USBL to the INS in each of the two alternative sensor-fusion filtering techniques—the loosely coupled version of the filter provides a position fix computed from the measured range and direction of the transponder (computed as described in Appendix A), whereas the new tightly coupled technique directly exploits the spatial information from the array, and provides the measured ranges from all receivers and all possible combinations of RDOA measurements.

respectively,

$$\begin{aligned}
\delta\dot{\mathbf{p}} &= \delta\mathbf{v},\\
\delta\dot{\mathbf{v}} &= -\mathcal{R}\delta\mathbf{b}_a - (\mathcal{R}\mathbf{a}_r)_\times\delta\boldsymbol{\lambda} + \mathcal{R}\mathbf{n}_a,\\
\delta\dot{\boldsymbol{\lambda}} &= -\mathcal{R}\delta\mathbf{b}_\omega + \mathcal{R}\mathbf{n}_\omega,\\
\delta\dot{\mathbf{b}}_a &= -\mathbf{n}_{b_a},\\
\delta\dot{\mathbf{b}}_\omega &= -\mathbf{n}_{b_\omega},
\end{aligned} \tag{6}$$

where the position and velocity linear errors are defined, respectively, by

$$\delta\mathbf{p} = \hat{\mathbf{p}} - \mathbf{p}, \qquad \delta\mathbf{v} = \hat{\mathbf{v}} - \mathbf{v}, \tag{7}$$

the matrix $\mathcal{R} \in SO(3)$ is the shorthand notation for the body $\{B\}$ to Earth $\{E\}$ coordinate frame rotation matrix ${}^E_B\mathbf{R}$, and the attitude error rotation vector $\delta\boldsymbol{\lambda}$ is defined by $\mathbf{R}(\delta\boldsymbol{\lambda}) \triangleq \hat{\mathcal{R}}\mathcal{R}^T$ and bears a first-order approximation,

$$\mathbf{R}(\delta\boldsymbol{\lambda}) \simeq \mathbf{I}_3 + [\delta\boldsymbol{\lambda}\times] \Rightarrow [\delta\boldsymbol{\lambda}\times] \simeq \hat{\mathcal{R}}\mathcal{R}^T - \mathbf{I}_3, \tag{8}$$

of the direction cosine matrix (DCM) form [see Appendix D for details on the usage of the DCM formulation in the INS, and in particular Eq. (D1)]. In particular, the proposed filter underlying the error model (6) includes the sensor's noise characteristics directly in the covariance matrices of the EKF and allows for attitude estimation using an unconstrained, locally linear, and nonsingular attitude parametrization. Once computed, the EKF error estimates are fed into the INS error correction routines as depicted in Figure 4. The attitude estimate, $\hat{\mathcal{R}}_k^-$, is compensated using the rotation error matrix $\mathbf{R}(\delta\boldsymbol{\lambda})$ definition, which yields

$$\hat{\mathcal{R}}_k^+ = \mathbf{R}_k^T(\delta\hat{\boldsymbol{\lambda}}_k)\hat{\mathcal{R}}_k^-,$$

where $\mathbf{R}_k^T(\delta\hat{\boldsymbol{\lambda}}_k)$ is parametrized by the rotation vector $\delta\hat{\boldsymbol{\lambda}}_k$ [according to Eq. (D1) in Appendix D]. The remaining state variables are linearly compensated using

$$\begin{aligned}
\hat{\mathbf{p}}_k^+ &= \hat{\mathbf{p}}_k^- - \delta\hat{\mathbf{p}}_k, \qquad & \hat{\mathbf{v}}_k^+ &= \hat{\mathbf{v}}_k^- - \delta\hat{\mathbf{v}}_k,\\
\hat{\mathbf{b}}_{a\,k}^+ &= \hat{\mathbf{b}}_{a\,k}^- - \delta\hat{\mathbf{b}}_{a\,k}, & \hat{\mathbf{b}}_{\omega\,k}^+ &= \hat{\mathbf{b}}_{\omega\,k}^- - \delta\hat{\mathbf{b}}_{\omega\,k}.
\end{aligned}$$

After the error correction procedure is completed, the EKF error estimates are reset. Therefore, linearization assumptions are kept valid and the attitude error rotation vector is stored in the $\hat{\mathcal{R}}_k^+$ matrix, preventing attitude error estimates to fall in singular configurations. At the start of the next computation cycle ($t = t_{k+1}$), the INS attitude and velocity/position updates are performed on the corrected estimates $(\hat{\boldsymbol{\lambda}}_k^+, \hat{\mathbf{v}}_k^+, \hat{\mathbf{p}}_k^+)$.

3.2. USBL Sensor-based INS Aiding

To tackle INS error buildup, the EKF relies on observations from external aiding sensors to accurately estimate the INS errors and correct them by relying on the direct feedback mechanism presented herein. This section introduces an external aiding technique based on the ranges and range-difference-of-arrival (RDOA) measured by a USBL, installed in an inverted configuration onboard the AUV (Vickery, 1998). A more detailed overview of the information flow, of both the state-of-the-art loosely coupled aiding technique and the novel tightly coupled filter, can be seen in the sequel in Figure 5.

3.2.1. Loosely Coupled USBL/INS

The transponder position fix, as measured by the USBL and described in Appendix A, can be described in body-fixed coordinates by

$$^{B}\mathbf{r}_r = \mathcal{R}^T(\mathbf{s} - \mathbf{p}) + \mathbf{n_r}, \tag{9}$$

where $\mathbf{s}$ is the transponder's position in an Earth-fixed coordinate frame, $\mathbf{p}$ is the position of the body-fixed frame origin in the Earth-fixed frame, and $\mathbf{n_r}$ represents the relative position measurement noise, characterized by taking into account the acoustic sensor noises and the USBL positioning system. The estimate of the relative position of the transponder in the body-fixed frame can be computed using the INS *a priori* estimates $\hat{\mathcal{R}}$ and $\hat{\mathbf{p}}$ as follows:

$$^{B}\hat{\mathbf{r}} = \hat{\mathcal{R}}^T(\mathbf{s} - \hat{\mathbf{p}}).$$

Using the position error definition (7) and replacing the rotation matrix $\mathcal{R}$ by the attitude error $\boldsymbol{\delta\lambda}$ approximation (8), manipulation of Eq. (9) yields

$$^{B}\mathbf{r}_r = {}^{B}\hat{\mathbf{r}} + \hat{\mathcal{R}}^T\boldsymbol{\delta}\mathbf{p} + (\hat{\mathcal{R}}^T\boldsymbol{\delta\lambda})_\times {}^{B}\hat{\mathbf{r}} + \hat{\mathcal{R}}^T(\boldsymbol{\delta\lambda})_\times\boldsymbol{\delta}\mathbf{p} + \mathbf{n_r}. \tag{10}$$

Thus, ignoring the second-order error term $\boldsymbol{\delta\lambda} \times \boldsymbol{\delta}\mathbf{p}$ and using the properties of the cross product and skew-symmetric matrices in Eq. (10) yields

$$^{B}\mathbf{r}_r = {}^{B}\hat{\mathbf{r}} + \hat{\mathcal{R}}^T\boldsymbol{\delta}\mathbf{p} - ({}^{B}\hat{\mathbf{r}})_\times\hat{\mathcal{R}}^T\boldsymbol{\delta\lambda} + \mathbf{n_r}.$$

The measurement residual used as observation in the EKF is given by the comparison between the measured transponder position fix and the estimated transponder position, leading to

$$\delta\mathbf{z}_r = {}^{B}\mathbf{r}_r - {}^{B}\hat{\mathbf{r}} = \hat{\mathcal{R}}^T\boldsymbol{\delta}\mathbf{p} - ({}^{B}\hat{\mathbf{r}})_\times\hat{\mathcal{R}}^T\boldsymbol{\delta\lambda} + \mathbf{n_r}. \tag{11}$$

Finally, in order to correctly describe $\mathbf{n_r}$, a stochastic linearization is performed on Eq. (11) (see Appendix B for additional details on the stochastic linearization performed on the residual position measurement).

3.2.2. Tightly Coupled USBL/INS

Classical loosely coupled strategies rely on position fixes computed prior to the filtering state, based on the same set of nonlinear range and RDOA measurements from the USBL subsystem. In such traditional approaches, the positions of the receivers onboard are not explicitly known by the filtering architecture. This section describes the proposed tightly coupled technique used to aid the INS with the USBL sensor information. The tightly coupled USBL/INS integration strategy directly exploits the acoustic array spatial information to calculate the distances from the transponders to each receiver on the USBL array, and it feeds this information directly into the EKF.

Using the position and attitude error definitions (7) and (8), respectively, yields for the range measurement of receiver i in Eq. (5)

$$\rho_i = \|\mathbf{s} - \hat{\mathbf{p}} + \boldsymbol{\delta}\mathbf{p} - \hat{\mathcal{R}}\mathbf{b}_i + (\boldsymbol{\delta\lambda})_\times\hat{\mathcal{R}}\mathbf{b}_i\|. \tag{12}$$

Using the properties of the cross product and skew-symmetric matrices in Eq. (12) yields

$$\rho_i = \|\mathbf{s} - \hat{\mathbf{p}} + \boldsymbol{\delta}\mathbf{p} - \hat{\mathcal{R}}\mathbf{b}_i - (\hat{\mathcal{R}}\mathbf{b}_i)_\times\boldsymbol{\delta\lambda}\|. \tag{13}$$

To improve performance, the EKF is directly fed with range measurements between the transponder and all receivers onboard, and also the RDOA between all receivers. Alternatively, the filter may be driven by one range observation and a set of independent RDOA measurements. The same set of observations that are used by the USBL subsystem to compute transponder position fixes are instead directly provided to the tightly coupled filter. Thus, the filter has direct knowledge of the receivers' positions on the local array and direct access to the raw range and RDOA measurements. Ultimately, this direct connection allows the filter to extract better raw and unmodified information from the acoustic measurements instead of relying on modified or transformed data from the USBL positioning schemes.

3.2.3. Additional Vector Observation

This section introduces an additional vector observation to improve the overall observability properties of the navigation system. The physical coupling between attitude and velocity errors, evidenced in Eq. (6), also enables the use of the USBL position fixes to partially estimate attitude errors. However, as this physical attachment is invariant in the body-fixed coordinate frame, the attitude error is not fully observable solely from the rate gyros, accelerometers, and USBL measurements.

As convincingly argued in Goshen-Meskin and Bar-Itzhack (1992) for observability analysis purposes, a GPS-only aided INS with bias estimation can be approximated by a concatenation of piecewise time-invariant systems, and, under that assumption, full observability is met by performing specific manoeuvres along the desired trajectory. Based on the observability theorem (Rugh, 1996), and as discussed in Morgado et al. (2006), a local weak observability analysis of the system reveals that either stopped or along a straight line path, full observability is only achieved using at least three transponders (on a nonsingular geometry) or two transponders and a magnetometer. Moreover, along curves, two transponders or one transponder and a magnetometer are sufficient to achieve full observability. Interestingly enough, specific in-flight alignment manoeuvres, such as transitions between straight paths to curves, excite the nonobservable directions of the system, turning the filter to full observability, as discussed in Goshen-Meskin and Bar-Itzhack (1992). Practical observability in real-world mission scenarios is nonetheless often achievable given that external environmental disturbances (for instance, underwater currents and the vehicle's own control action to counteract disturbances) excite some unobservable directions. However, each specific manoeuvre often includes a subset of unobservable states, and hence

additional aiding sensors are of interest to improve full state estimation. Recent work by Koifman and Bar-Itzhack (1999) and Vasconcelos et al. (2011) has been directed toward the inclusion of vehicle dynamic information to strengthen the system observability.

Thus, the required extra attitude measurement can be drawn from observations of Earth-fixed reference vectors, with onboard sensors that measure the same quantity, in body-fixed coordinates, as follows:

$$^{B}\mathbf{x}_r = \mathcal{R}^{T}\,{}^{E}\mathbf{x} + \mathbf{n}_x,$$

where $^{E}\mathbf{x}$ is the nominal reference vector in Earth-fixed coordinates, assumed known and locally constant, and $\mathbf{n}_x$ is the vector measurement noise. The vector-aiding measurement residual is computed by comparing this vector observation to the same estimated quantity given the INS *a priori* attitude estimate $\hat{\mathcal{R}}$ as

$$^{B}\mathbf{z}_c = {}^{B}\mathbf{x}_r - \hat{\mathcal{R}}^{T}\,{}^{E}\mathbf{x} = \hat{\mathcal{R}}^{T}(\hat{\mathcal{R}}\mathcal{R}^{T} - \mathbf{I})^{E}\mathbf{x} + \mathbf{n}_x \tag{14}$$

in body-fixed coordinates, or in Earth-fixed coordinates as

$$^{E}\mathbf{z}_c = \hat{\mathcal{R}}\,{}^{B}\mathbf{x}_r - {}^{E}\mathbf{x} = (\hat{\mathcal{R}}\mathcal{R}^{T} - \mathbf{I})^{E}\mathbf{x} + \hat{\mathcal{R}}\mathbf{n}_x. \tag{15}$$

Using the attitude error approximation (8) and the properties of the cross product in Eqs. (14) and (15) yields

$$^{B}\mathbf{z}_c = -\hat{\mathcal{R}}^{T}({}^{E}\mathbf{x})_{\times}\boldsymbol{\delta\lambda} + \mathbf{n}_x \tag{16}$$

in body-fixed coordinates, or in Earth-fixed coordinates as

$$^{E}\mathbf{z}_c = -({}^{E}\mathbf{x})_{\times}\boldsymbol{\delta\lambda} + \hat{\mathcal{R}}\mathbf{n}_x. \tag{17}$$

The vector observation model in Eq. (16) or in Eq. (17) can be particularized to any suitable vector sensor, such as gyroscopic inclinometers and magnetometers. Other examples of vector observations can be found in the low-frequency content of bias-compensated triads of a fiber optic rate gyroscope (FOG) that are able to measure Earth's rotation vector, and in image- or sonar-based algorithms that extract vector features from the environment. Magnetometers are typically used in the literature as heading sensors providing only one angle measurement, whereas using a triad of magnetometers allows for the exploitation of all information available from Earth's magnetic field—i.e. two angles when the local magnetic model includes both the magnetic declination and inclination. Thus, a triad of magnetometers is adopted in this work as a vector observation sensor providing measurements of the Earth's magnetic field in body-fixed coordinates,

$$^{B}\mathbf{m}_r = \mathcal{R}^{T}\,{}^{E}\mathbf{m} + \mathbf{n}_x,$$

where $^{E}\mathbf{m}$ is the nominal local magnetic field vector in Earth-fixed coordinates, assumed known and locally constant, and $\mathbf{n}_m$ is the magnetometer measurement noise. The magnetometers are considered to be calibrated and compensated for bias, scale factors, and nonorthogonality of the input axis prior to each mission, using, for instance, attitude-independent batch processing methods (Alonso and Shuster, 2002). Applying the observation models in Eqs. (16) and (17) to the magnetometers triad yields

$$^{B}\mathbf{z}_c = -\hat{\mathcal{R}}^{T}({}^{E}\mathbf{m})_{\times}\boldsymbol{\delta\lambda} + \mathbf{n}_m \tag{18}$$

in body-fixed coordinates, or in Earth-fixed coordinates as

$$^{E}\mathbf{z}_c = -({}^{E}\mathbf{m})_{\times}\boldsymbol{\delta\lambda} + \hat{\mathcal{R}}\mathbf{n}_m. \tag{19}$$

3.3. Implementation

This section presents the implementation details of the proposed filters in a stochastic filtering setup, particularly suited to be implemented in an EKF in a direct-feedback structure as presented herein. A comparison of the information flow of both the state-of-the-art loosely coupled aiding technique and the novel tightly coupled filter can be seen in Figure 5.

Without loss of generality, let any continuous-time state space model be described as

$$\begin{cases}\dot{\mathbf{x}}_c = \mathbf{F}_c(\mathbf{x}_c)\mathbf{x}_c + \mathbf{G}_c(\mathbf{x}_c)\mathbf{n}_{\mathbf{x}_c} + \mathbf{u}_c,\\ \mathbf{z}_c = \mathbf{H}_c(\mathbf{x}_c)\mathbf{x}_c + \mathbf{n}_{\mathbf{z}_c},\end{cases}$$

where $\mathbf{x}_c$ is the state vector, $\mathbf{F}_c$ is the state dynamics matrix, $\mathbf{n}_{\mathbf{x}_c}$ is the state noise, $\mathbf{G}_c$ is the matrix that links the state noise to the state evolution, $\mathbf{u}_c$ is a vector that represents the known deterministic inputs, and $\mathbf{z}_c$ represents the vector measurements that relate to the state vector through the matrix $\mathbf{H}_c$ and is disturbed by the observation noise vector $\mathbf{n}_{\mathbf{z}_c}$. The state and measurement noises are considered to be zero-mean, uncorrelated, additive white Gaussian noise (AWGN) processes, and with covariance matrices $\mathbf{Q}_c$ and $\mathbf{R}_c$ such that

$$\begin{aligned} E\left\{\mathbf{n}_{\mathbf{x}_c}(t)\mathbf{n}_{\mathbf{x}_c}(\tau)^{T}\right\} &= \mathbf{Q}_c(t)\delta(t-\tau),\\ E\left\{\mathbf{n}_{\mathbf{z}_c}(t)\mathbf{n}_{\mathbf{z}_c}(\tau)^{T}\right\} &= \mathbf{R}_c(t)\delta(t-\tau).\end{aligned} \tag{20}$$

Specifying for the navigation system at hand, the state vector to be estimated consists of the inertial errors in position, velocity, and attitude, and it also includes the inertial sensor biases offsets as described in Section 3.1,

$$\mathbf{x}_c = \delta\mathbf{x}_{\text{ins}} = \left[\delta\mathbf{p}^{T}\ \delta\mathbf{v}^{T}\ \delta\boldsymbol{\lambda}^{T}\ \delta\mathbf{b}_{\mathbf{a}}{}^{T}\ \delta\mathbf{b}_{\boldsymbol{\omega}}{}^{T}\right]^{T} \quad \in \mathbb{R}^{15},$$

and the state model of the first-order INS error Eqs. (6) given by

$$\dot{\mathbf{x}}_c = \delta\dot{\mathbf{x}}_{\mathbf{ins}} = \mathbf{F}_{\mathbf{ins}}(\hat{\mathbf{x}})\delta\mathbf{x}_{\mathbf{ins}} + \mathbf{G}_{\mathbf{ins}}(\hat{\mathbf{x}})\mathbf{n}_{\mathbf{ins}},$$

where $\mathbf{n}_{\mathbf{ins}} = \left[\mathbf{n}_{\mathbf{p}}{}^{T}\ \mathbf{n}_{\mathbf{a}}{}^{T}\ \mathbf{n}_{\boldsymbol{\omega}}{}^{T}\ \mathbf{n}_{\mathbf{b}_{\mathbf{a}}}{}^{T}\ \mathbf{n}_{\mathbf{b}_{\boldsymbol{\omega}}}{}^{T}\right]^{T} \in \mathbb{R}^{15}$, $\mathbf{n}_{\mathbf{p}} \sim \mathcal{N}(\mathbf{0}, \boldsymbol{\Sigma}_{\mathbf{p}})$ is a fictitious white-noise process associated with the position integration error. This fictitious noise serves to account for unmodeled dynamics in the filters, and it also acts as a tuning knob on the filter, allowing for the tuning of the frequency response of the filter from the inputs to the position estimate. The matrices $\mathbf{F}_{\mathbf{ins}} \in \mathbb{R}^{15\times 15}$ and

$\mathbf{G_{ins}} \in \mathbb{R}^{15\times15}$ are given by

$$\mathbf{F_{ins}}(\hat{\mathbf{x}}) = \begin{bmatrix} \mathbf{0} & \mathbf{I}_3 & \mathbf{0} & \mathbf{0} & \mathbf{0} \\ \mathbf{0} & \mathbf{0} & -(\hat{\mathcal{R}}\mathbf{a_r})_\times & -\hat{\mathcal{R}} & \mathbf{0} \\ \mathbf{0} & \mathbf{0} & \mathbf{0} & \mathbf{0} & -\hat{\mathcal{R}} \\ \mathbf{0} & \mathbf{0} & \mathbf{0} & \mathbf{0} & \mathbf{0} \\ \mathbf{0} & \mathbf{0} & \mathbf{0} & \mathbf{0} & \mathbf{0} \end{bmatrix},$$

$$\mathbf{G_{ins}}(\hat{\mathbf{x}}) = \mathrm{diag}(\mathbf{I}_3, \hat{\mathcal{R}}, \hat{\mathcal{R}}, -\mathbf{I}_3, -\mathbf{I}_3),$$

where $\mathrm{diag}(\cdot, \ldots, \cdot)$ represents a block diagonal matrix. The state noise covariance matrix is given by

$$\mathbf{Q_{ins}} = \mathrm{diag}(\mathbf{\Sigma_p}, \mathbf{\Sigma_a}, \mathbf{\Sigma_\omega}, \mathbf{\Sigma_{b_a}}, \mathbf{\Sigma_{b_\omega}}) \in \mathbb{R}^{15\times15}.$$

3.3.1. Magnetometer Vector Aiding

Although the measurement residuals (18) and (19) describe the same attitude information, the linearized measurement matrix for Eq. (19) is constant and the components of $\boldsymbol{\delta\lambda}$ can be related directly with those of ${}^E\mathbf{m}$. The observation matrix for the magnetometer vector observation is then given by

$$\mathbf{H}_{c\,\mathrm{mag}} = \begin{bmatrix} \mathbf{0} & \mathbf{0} & -({}^E\mathbf{m})_\times & \mathbf{0}_{3\times9} \end{bmatrix} \in \mathbb{R}^{3\times15}.$$

The measurement noise covariance matrix comes as

$$\mathbf{R}_{c\,\mathrm{mag}} = \hat{\mathcal{R}}\mathbf{\Sigma}_m\hat{\mathcal{R}}^T \in \mathbb{R}^{3\times3},$$

where $\mathbf{\Sigma}_m$ is the covariance matrix of the white Gaussian magnetometer noise $\mathbf{n}_m \sim \mathcal{N}(\mathbf{0}, \mathbf{\Sigma}_m)$.

3.3.2. Loosely Coupled USBL

The loosely coupled filter uses the USBL position fixes, computed using the planar-wave approximation as described in Appendix A, which are fed to the EKF to correct the inertial errors in the INS and estimate the inertial sensor biases. The EKF computes the measurement residuals using Eq. (11), where a stochastic linearization is performed to correctly describe the positioning error $\mathbf{n_r}$. Thus, the set of measurements provided to the loosely coupled filter is given by

$$\mathbf{z}_{c\,\mathrm{USBL}} = \delta\mathbf{z}_r = {}^B\mathbf{r}_r - {}^B\hat{\mathbf{r}}.$$

Taking into account Eq. (11), the measurement Jacobian $\mathbf{H}_{c\,\mathrm{USBL}} \in \mathbb{R}^{3\times15}$ is given by

$$\mathbf{H}_{c\,\mathrm{USBL}} = \begin{bmatrix} \hat{\mathcal{R}}^T & \mathbf{0}_{3\times3} & -({}^B\hat{\mathbf{r}})_\times\hat{\mathcal{R}}^T & \mathbf{0}_{3\times3} & \mathbf{0}_{3\times3} \end{bmatrix}.$$

Based on a stochastic linearization of the USBL position fix, described in Appendix B, the covariance matrix of the observation noise is given by

$$\mathbf{R}_{c\,\mathrm{USBL}} = \begin{bmatrix} V_{xx} & V_{xy} & V_{xz} \\ V_{yx} & V_{yy} & V_{yz} \\ V_{zx} & V_{zy} & V_{zz} \end{bmatrix},$$

where the matrix elements V_{kj} with $k = x, y, z$ and $j = x, y, z$ are given by

$$\begin{aligned} V_{kj} &= E\{(g(\rho, d_k) - E\{g(\rho, d_k)\})\}\{(g(\rho, d_j) - E\{g(\rho, d_j)\})\} \\ &= \bar{d}_k\bar{d}_j E\{(\rho - \bar{\rho})^2\} + \bar{d}_k\bar{\rho}E\{(\rho - \bar{\rho})(d_j - \bar{d}_j)\} \\ &\quad + \bar{d}_j\bar{\rho}E\{(\rho - \bar{\rho})(d_k - \bar{d}_k)\} \\ &\quad + \bar{\rho}^2E\{(d_k - \bar{d}_k)(d_j - \bar{d}_j)\}. \end{aligned}$$

3.3.3. Tightly Coupled USBL

The tightly coupled USBL provides measurements of the ranges between the transponder and the onboard receivers, which are described using the INS estimates by Eq. (13). The EKF is also fed with the set of RDOA between the receivers with a higher precision. Thus, the set of measurements provided to the filter is given by the residuals

$$\mathbf{z}_{c\,\mathrm{USBL}} = \begin{bmatrix} \rho_1 \cdots \rho_{n_m} \ \rho_1 - \rho_2 \ \rho_2 - \rho_3 \cdots \rho_{n_r-1} - \rho_{n_r} \end{bmatrix}^T,$$

where n_m is the number of stand-alone measured ranges, either one or the full set of n_r measurements ($n_m \leq n_r$), and the observation Jacobian is given by

$$\begin{aligned} &\mathbf{H}_{c\,\mathrm{USBL}} \\ &= \begin{bmatrix} \mathbf{H}_{u,1}{}^T \cdots \mathbf{H}_{u,n_m}{}^T \ \mathbf{H}_{u,1}{}^T - \mathbf{H}_{u,2}{}^T \cdots \mathbf{H}_{u,n_r-1}{}^T - \mathbf{H}_{u,n_r}{}^T \end{bmatrix}^T, \end{aligned}$$

where each component $\mathbf{H}_{u,i} \in \mathbb{R}^{1\times15}$ is given by

$$\begin{aligned} &\mathbf{H}_{u,i} \\ &= \begin{bmatrix} \dfrac{(\mathbf{s} - \hat{\mathbf{p}} - \hat{\mathcal{R}}\mathbf{b}_i)^T}{\|\mathbf{s} - \hat{\mathbf{p}} - \hat{\mathcal{R}}\mathbf{b}_i\|} \ \mathbf{0}_{1\times3} \ \dfrac{-(\mathbf{s} - \hat{\mathbf{p}} - \hat{\mathcal{R}}\mathbf{b}_i)^T\hat{\mathcal{R}}(\mathbf{b}_i)_\times\hat{\mathcal{R}}^T}{\|\mathbf{s} - \hat{\mathbf{p}} - \hat{\mathcal{R}}\mathbf{b}_i\|} \ \mathbf{0}_{1\times3} \ \mathbf{0}_{1\times3} \end{bmatrix}, \end{aligned}$$

which is only well-defined for $\hat{\rho}_i = \|\mathbf{s} - \hat{\mathbf{p}} - \hat{\mathcal{R}}\mathbf{b}_i\| > 0$. The measurement covariance matrix is defined as

$$\mathbf{R}_{c\,\mathrm{USBL}} = \begin{bmatrix} \sigma_c^2\mathbf{1}_{n_m\times n_m} + \sigma_d^2\mathbf{I}_{n_m} & \mathbf{R}_{\mathrm{cross}}^T \\ \mathbf{R}_{\mathrm{cross}} & 2\sigma_d^2\mathbf{I}_{n_c} \end{bmatrix},$$

where n_c is the number of combinations used for the set of RDOA measurements, with $n_c \leq C_2^{n_r} = n_r(n_r-1)/2$. The higher precision at which the RDOA are measured compared to the actual ranges is expressed in the fact that $\sigma_c^2 \gg \sigma_d^2$. The covariance matrix $\mathbf{R}_{\mathrm{cross}}$ is given by

$$\mathbf{R}_{\mathrm{cross}} = \begin{bmatrix} \sigma_d^2 & -\sigma_d^2 & 0 & 0 & \cdots & 0 \\ \sigma_d^2 & 0 & -\sigma_d^2 & 0 & \cdots & 0 \\ & & & \vdots & & \\ 0 & \cdots & 0 & \sigma_d^2 & 0 & -\sigma_d^2 \\ 0 & \cdots & 0 & 0 & \sigma_d^2 & -\sigma_d^2 \end{bmatrix}.$$

3.3.4. Discretization

The implementation of the state-space model in a discrete-time setting is easily obtained resorting to the classical zero-order hold discretization method described in Gelb (1974),

in which the inputs are regarded as constant during sample times of the discrete filter. The system state is given by the INS error model $\mathbf{x}_c = \delta\mathbf{x}_{\mathbf{ins}}$, and the remaining quantities are set by $\mathbf{n}_{\mathbf{x_c}} = \mathbf{n}_{\mathbf{ins}}$, $\mathbf{F}_c(\hat{\mathbf{x}}) = \mathbf{F}_{\mathbf{ins}}(\hat{\mathbf{x}})$, $\mathbf{G}_c(\hat{\mathbf{x}}) = \mathbf{G}_{\mathbf{ins}}(\hat{\mathbf{x}})$. The state covariance in Eq. (20) is given by $\mathbf{Q}_c = \mathbf{Q}_{\mathbf{ins}}$. The discrete state transition matrix is approximated by

$$\boldsymbol{\Phi}_k(t_{k+1}, t_k) \approx e^{\mathbf{F}_k(t_{k+1}-t_k)},$$

where $\mathbf{F}_k = \mathbf{F}_c|_{t=t_k}(\hat{\mathbf{x}}_k^+)$ is evaluated at the updated state estimate $\hat{\mathbf{x}}_k^+$, and $e^{(\cdot)}$ represents the matrix exponential. The measurements are provided to the filter by stacking the observations from the magnetometer and the USBL when each is available. The processing of the EKF allows for either a batch-processing of the observations from several asynchronous sensors or from stacking the observations in the same measurement vector and adjusting the corresponding measurement covariance matrices. The state estimate is updated using the standard EKF state update equation

$$\hat{\mathbf{x}}_k^+ = \hat{\mathbf{x}}_k^- + \mathbf{K}_k\left(\mathbf{z}_k - \mathbf{h}\left(\hat{\mathbf{x}}_k^-\right)\right),$$

where $\mathbf{K}_k$ is the Kalman matrix gain, $\hat{\mathbf{x}}_k^+$ is the updated state estimate, $\hat{\mathbf{x}}_k^-$ is the prior state estimate, $\mathbf{z}_k$ are the aiding sensor observations, and $\mathbf{h}\left(\mathbf{x}_k^-\right)$ is the set of predicted observations, evaluated at the prior state estimate. The Kalman gain and remaining quantities are calculated using the standard EKF update and propagation equations (Gelb, 1974),

$$\begin{aligned}
\mathbf{K}_k &= \left(\mathbf{P}_k^-\mathbf{H}_k^T + \mathbf{C}_k\right)\left(\mathbf{H}_k\mathbf{P}_k^-\mathbf{H}_k^T + \mathbf{R}_k + \mathbf{H}_k\mathbf{C}_k + \mathbf{C}_k{}^T\mathbf{H}_k^T\right)^{-1},\\
\mathbf{P}_k^+ &= (\mathbf{I} - \mathbf{K}\mathbf{H}_k)\mathbf{P}_k^- - \mathbf{K}_k\mathbf{C}_k^T,\\
\mathbf{P}_{k+1}^- &= \boldsymbol{\phi}_k\mathbf{P}_k^+\boldsymbol{\phi}_k^T + \mathbf{Q}_k,
\end{aligned}$$

where $\mathbf{P}_k^-$ is the prior state estimation error covariance matrix, $\mathbf{P}_k^+$ is the posterior corrected state estimation error covariance matrix, and $\mathbf{H}_k$ is the Jacobian matrix of the nonlinear observation equation $\mathbf{h}\left(\mathbf{x}_k^-\right)$ evaluated at the prior state estimate as presented in the previous sections. The matrices $\mathbf{R}_k$ and $\mathbf{Q}_k$ are the discrete equivalents of, respectively, the observations and state noise covariance matrices from sample time t_k to t_{k+1}. Under the zero-order hold approximation, $\mathbf{R}_k$ and $\mathbf{Q}_k$ are given by (Gelb, 1974)

$$\begin{aligned}
\mathbf{Q}_k &\approxeq \left[\mathbf{G}_k\mathbf{Q}_c|_{t=t_k}\mathbf{G}_k^T\right]T_s,\\
\mathbf{R}_k &\approxeq \mathbf{R}_c|_{t=t_k}/T_s,
\end{aligned}$$

where $\mathbf{G}_k = \mathbf{G}_c|_{t=t_k}$, and $T_s = (t_{k+1} - t_k)$ is the filter sample time. As described in Section 3.1, the estimated INS errors are passed on to the error-correction routines in the INS algorithm and reset in the EKF maintaining valid all previous linearisation assumptions.

4. NUMERICAL SIMULATION RESULTS AND PERFORMANCE EVALUATION

The overall navigation system performance was assessed in simulation using extensive Monte-Carlo simulations in which the filtering setup and all the sensors are exposed to different initial conditions and noise sequences. Prior to detailing the numerical simulation tests and characteristics, a brief overview of the theoretical bounds used in this work to assess the performance of the proposed techniques is presented below.

Theoretical performance bounds have long been pursued as an important design tool that helps gauge the attainable performance by any estimator based on preset conditions of process observations and noise. This kind of bound also provides an assessment of whether imposed performance specifications are feasible. A commonly used lower bound for time-invariant statistical models is the Cramér-Rao lower bound, which provides a lower bound on the estimation error of any estimator of an unknown constant parameter of that particular statistical model. An analogous bound for random parameters for nonlinear, nonstationary system models, referred to as the Bayesian Cramér-Rao lower bound (BCRB), was first derived in Van Trees (1966) and carefully reviewed in Van Trees (1968) and Van Trees and Bell (2007). A discrete-time version, known as posterior Cramér-Rao lower bound (PCRLB), was introduced in Van Trees (1968) and has proven to be a valuable analysis tool to assess the performance of discrete-time dynamical estimators. It is also suitable for nonlinear, nonstationary dynamical systems, as is the case of the work presented herein, and it was recently used for point and extended target tracking (Zhong et al., 2010). The solution proposed in Van Trees (1968) did not allow, however, for an efficient computation of the bound, and a recursive method for an efficient computation of the PCRLB for the discrete-time case was presented in Tichavskỳ et al. (1998). Readers not familiar with the theory beyond the PCRB should follow the review presented in Tichavskỳ et al. (1998) and references therein. An overview of the PCRLB applied to this work is provided in Appendix C.

The USBL receiving array has a baseline of approximately 30 cm and is composed of four receivers that are installed in the positions given by $\mathbf{b}_1 = [\,0.2\ -0.15\ 0\,]^T$ m, $\mathbf{b}_2 = [\,0.2\ 0.15\ 0\,]^T$ m, $\mathbf{b}_3 = [\,0.4\ 0\ 0.15\,]^T$ m, and $\mathbf{b}_4 = [\,0.4\ 0\ -0.15\,]^T$ m, with respect to the body-fixed coordinate frame $\{B\}$, where the inertial measurement unit (IMU) is also installed in a strap-down configuration. A schematic representation of the USBL array can be found in Figure 5, in Section 3, and the actual array can be seen in the sequel in Figure 11(b), in Section 5. The INS provides open-loop integrated estimates of the platform position, velocity, and attitude with a frequency of 50 Hz, and the triad of accelerometers is inspired by a realistic, commercially available sensor package, the Crossbow® CXL02TG3 triaxial accelerometer, considered to provide specific force

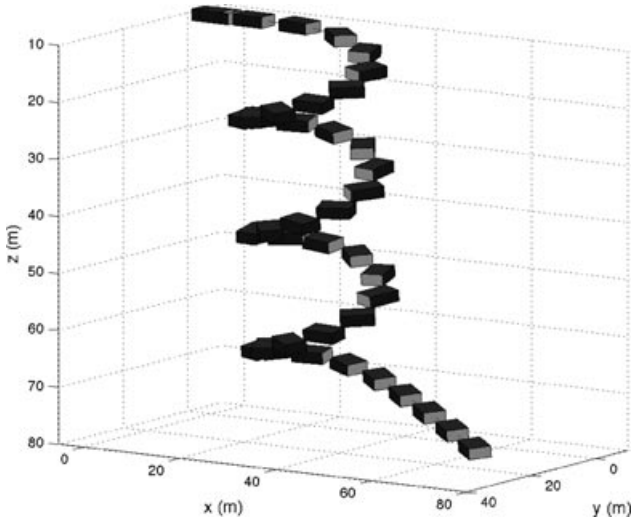

Figure 6. Vehicle trajectory.

measurements corrupted by additive uncorrelated, biased white Gaussian noise, with a standard deviation of 0.6 mg (that is, 5.886×10^{-3} m/s^2 for a gravity constant of $g \approx 9.81$ m/s^2). The rate gyros are also inspired by a realistic sensor package, the Silicon Sensing CRS03 triaxial rate gyro, and are thus considered to be disturbed by additive, uncorrelated, biased white Gaussian noise, with a standard deviation of 0.05 deg/s. A magnetometer is also used in the proposed solution, as described in Section 3.2.3, and inspired by the commercially available Crossbow® CXM113 triaxial magnetometer, which is assumed to be calibrated for bias, scale factors, and nonorthogonality of the input axis, but is disturbed by AWGN with zero-mean and standard deviation of 60 μG. The range measurements between the transponder and the reference receiver (receiver 1) are considered to be disturbed by additive, zero-mean white Gaussian noise, with 0.3 m standard deviation, while the RDOA between receiver 1 and the other three receivers is considered to be measured with an accuracy of 6 mm. The transponder is located in local inertial coordinates at $\mathbf{s} = [\,0\ 100\ 0\,]^T$ m. The vehicle describes the trajectory depicted in Figure 6, and the inertial sensor biases were modeled in simulation as unknown constants different from zero, although in the filters the corresponding state variables are tuned to be slowly time varying. In practice, the inertial sensor biases are actually slowly time varying with unknown time constants, as will be seen in the experimental results analysis in Section 6.

To correctly compute the PCRLB for the specific navigation systems in the analysis herein, the numerical integration algorithms are executed in a direct-feedback setting without the EKF in the loop for several Monte-Carlo realizations of the inertial sensors AWGN disturbances. In each integration step, the errors that arise from the inertial algorithms are recorded for posterior evaluation of the PCRLB and reset in the correction routines. Using this setup, the evaluated PCRLB assesses the attainable performance of any estimator that is placed in the direct-feedback loop. The bound was computed with several points, in particular for

$$M = \{10, 20, 100, 200, 300, 400, 500, 600, 700, 800, 900, 1{,}000\}, \tag{21}$$

with $n = 12$ elements and for each value $i < n$ in the set, compared against the bound computed with 1,000 points (the last value of M). Thus, the plot in Figure 7 compares the norm of the error of computing the bound with the first $n - 1$ points of the set M in (21) compared to the bound computed with 1,000 points (the last value of M). As illustrated in Figure 7, the bound computation error changes significantly when computed with 100 points relatively to 10 or 20 points. The error to the bound computed with 1,000 points does not change significantly when computed with either 800 or 900 points, leading to the conclusion that computing the bound with 900 points is similar to computing with 800, which indicates that a tight bound has been found. The lower bound computed herein, i.e., the PCRLB, represents the best-case scenario of the attainable performance by any estimator given the trajectory of the vehicle and the available sensors. This relation is well established by the theory behind the PCRLB, briefly described in Appendix C. Instead of having two separate bounds for each USBL observation model—the loosely coupled and the tightly coupled—a single bound that uses the full nonlinear range equations between the vehicle and the transponder is considered in the sequel. The reasoning behind the usage of this single bound to gauge the attainable performance of both strategies lies in the fact that the loosely coupled filter uses the same acoustic hydrophones as the tightly coupled solution to compute the position of the transponder. Ultimately, the loosely coupled transponder positioning computation applies a transformation to the underlying raw acoustic data, which is in part responsible for the difference of performance between the two strategies, which is what this study seeks to assess.

The loosely coupled and the tightly coupled fusion techniques were compared to the PCRLB resorting to $N = 100$ Monte-Carlo runs in which all the sensors are subject to different noise sequences and the filtering setup is exposed to different initial conditions drawn from a normal Gaussian distribution with zero mean and standard deviations given by 5 m in position error, 0.5 m/s in velocity error, 1 deg in attitude error; 0.0785 m/s^2 in accelerometer bias misalignment, and $10/3$ deg/s in rate gyro bias misalignment. The mean position error from the Monte-Carlo evaluation of both strategies is compared in Figure 8(a) where it can be confirmed that both strategies are unbiased estimators for position. The performance enhancement of the tightly coupled strategy is evident from the root-mean-square (RMS) position estimation error comparison in

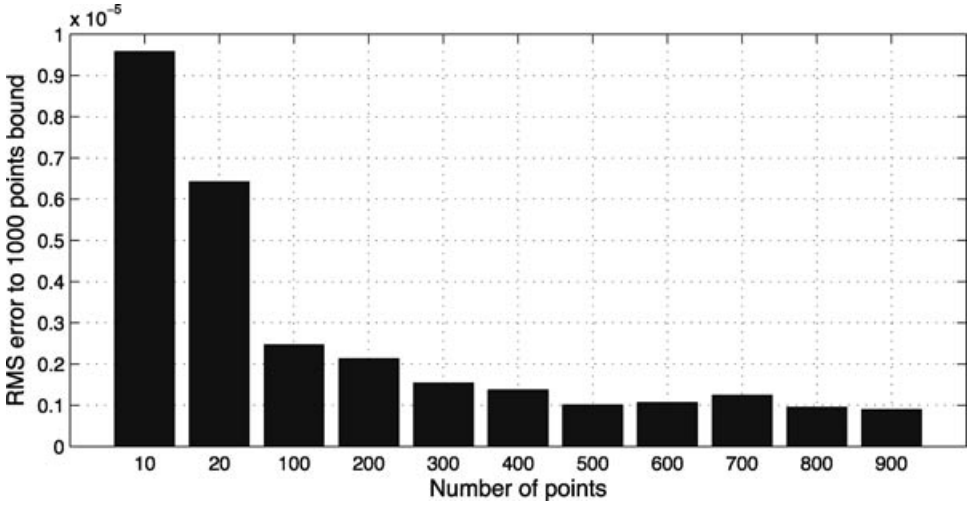

Figure 7. Posterior Cramér-Rao bound Monte-Carlo evaluation with several evaluation points. The plot compares the norm of the error of computing the bound with the first $n-1$ points of the set M in Eq. (21) compared to the bound computed with 1,000 points (the last point of M). The bound computation error changes significantly when computed with 100 points relative to 10 or 20 points. The error to the bound computed with 1,000 points does not change significantly when computed with either 800 or 900 points, leading to the conclusion that computing the bound with 900 points is similar to computing with 800, which indicates that a tight bound has been found.

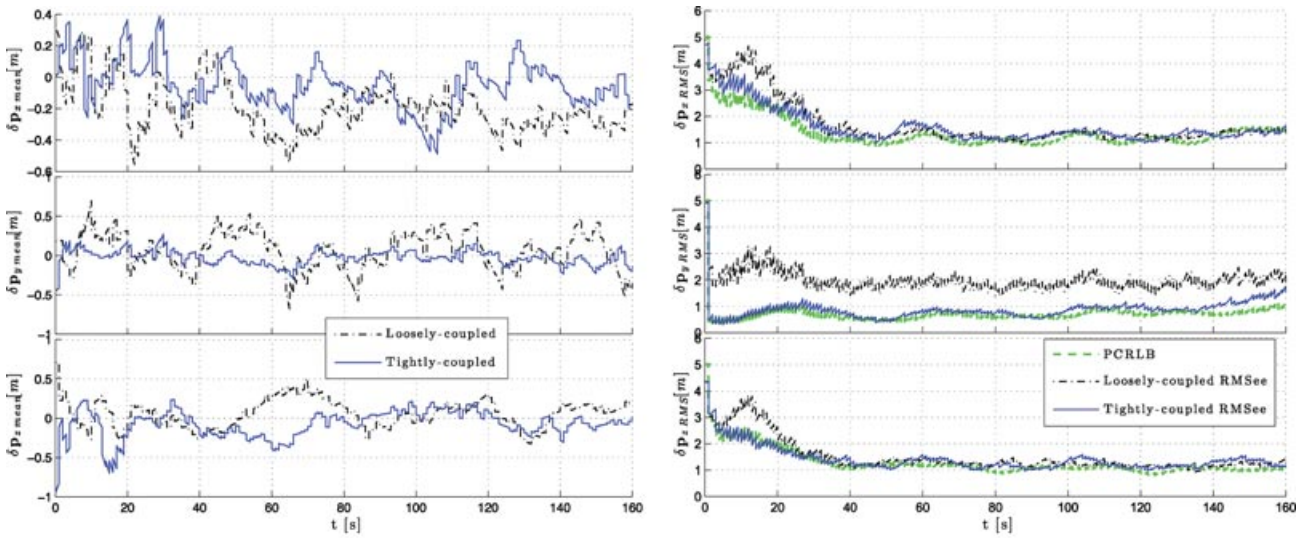

Figure 8. Position mean and root-mean-square (RMS) estimation error for tightly coupled *vs.* loosely coupled comparison with $N = 100$ Monte-Carlo runs. The performance enhancement in the position estimation accuracy of the tightly coupled strategy is evident from the comparison with the loosely coupled one, where the tightly coupled EKF is shown to operate near the PCRLB as opposed to the loosely coupled EKF.

Figure 8(b). The tightly coupled EKF is shown to clearly operate near the PCRLB as opposed to the loosely coupled solution, with improved estimation accuracy.

The enhancement in position estimation performance is further evidenced through the analysis of the norm of the position error in Figure 9. The remaining quantities (velocity, attitude and inertial sensor biases) are also shown to bear clear improvements with the novel tightly coupled fusion technique when compared to the loosely coupled fusion classical strategy. Assuming the ergodicity hypothesis, the steady-state estimation error for the remaining quantities is summarized in Table I for the velocity and attitude

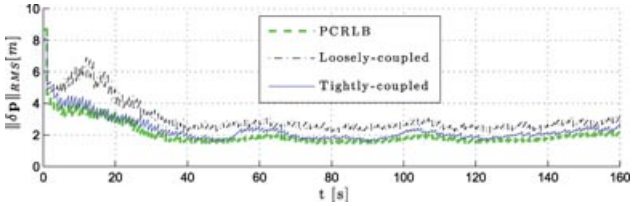

Figure 9. Root-mean-square (RMS) of the norm of the position estimation error for tightly coupled *vs.* loosely coupled comparison with $N = 100$ Monte-Carlo runs. Notice the sawtooth pattern that is caused by the difference in update rates between the acoustic corrections at 1 Hz and the open-loop INS numerical integration routines at 50 Hz.

Table I. Steady-state velocity and attitude estimation error for tightly coupled *vs.* loosely coupled comparison with $N = 100$ Monte-Carlo runs.

	Velocity error $\|\delta\mathbf{v}\|$ (ms^{-1})		Attitude error $\|\delta\lambda\|$ (rad)	
Filter coupling	Average	RMS	Average	RMS
Loosely coupled	$6.6e-02$	0.180	$1.4e-03$	$5.7e-05$
Tightly coupled	$3.4e-02$	0.045	$7.5e-04$	$4.3e-05$

Table II. Steady-state inertial sensors bias estimation error for tightly coupled *vs.* loosely coupled comparison with $N = 100$ Monte-Carlo runs.

	R.G. Bias $\|\delta\mathbf{b}_\omega\|$ (rad s^{-1})		Accel. Bias $\|\delta\mathbf{b}_\mathbf{a}\|$ (ms^{-2})	
Filter coupling	Average	RMS	Average	RMS
Loosely coupled	$4.5e-05$	$2.2e-08$	$1.2e-03$	$1.3e-04$
Tightly coupled	$2.7e-05$	$1.9e-08$	$9.1e-04$	$1.4e-04$

estimation errors, and in Table II for the inertial sensor biases estimation errors.

The performance enhancement of the novel tightly coupled technique to directly merge the range and RDOA observations of an USBL acoustic positioning system into the direct-feedback EKF (see Figure 4 in Section 3) is evident from the numerical simulation results presented herein.

5. EXPERIMENTAL SYSTEM DESIGN

The marine habitat naturally poses a huge challenge for systems development mainly due to its harsh environment, in which marine robotic vehicles have to withstand high pressures. Several capable and high-performance navigation systems are readily available on the market, such as the PHINS^{TM} underwater INS, the combined USBL+INS+GPS surface tracking system GAPS^{TM}, and the long-range USBL tracking device POSIDONIA^{TM}, all from IXSEA$^{®}$indexcommercially available products. LinkQuest$^{®}$ also provides lower-performance and lower-cost USBL systems that can also be submerged. Commercially available solutions, however, do not often allow direct access to the travel times of the acoustic waves on the array receivers. Moreover, commercial inertial navigation systems often have their outputs downgraded due to export regulations. The combination of these facts, and the prohibitively high cost of current commercial solutions, stifle the design of low-cost marine robotic vehicles.

This section is directed toward the development of a high-performance, low-cost navigation research system that meets the need of providing direct access to the time-of-arrival (TOA) of the acoustic waves on the array receivers, bearing the valuable knowledge inherent to the assembly and design of such a system. An architecture for the open prototype is proposed, the acoustic array design is discussed, the inertial sensor package is presented, supporting acoustic signals to be used are briefly enumerated, and implementation issues are detailed. As a by-product, the system also includes the design of a transponder that replies to the interrogations sent out by the integrated USBL/INS system. An interesting and similar inverted USBL design was presented in Jaffré et al. (2005); however, this design does not include the tightly coupled features presented herein as it requires external attitude measurements for global navigation capabilities. An alternative navigation system design can be found in Yun et al. (1999), in which the vehicle navigates underwater using an INS and surfaces sporadically to get GPS position fixes and correct the errors of the INS. A summary of the design presented herein was previously presented by Morgado et al. (2010).

The proposed USBL/INS hardware and software architecture consists mainly of two major stand-alone systems: the first is the ensemble between the acoustic array and the inertial unit, providing acoustic signal acquisition and processing. The latter is a transponder that scouts for signals sent by the USBL array and replies after a previously stipulated elapsed time in order for the array to compute RTT to the transponder. In this section, all proposed systems and signal processing techniques are presented.

5.1. USBL/INS System Overview

The integrated USBL/INS hardware is housed in an aluminum pressure tube capable of withstanding pressures up to 600 m (tested in a water pressure chamber). The USBL array is built using Bosch-Rexroth$^{®}$ aluminum rods and connections, which allow for a highly configurable array structure for optimal design during the evaluation and testing phases. The array is composed of four preamplified HTI$^{®}$ -96-MIN (4) hydrophones placed in a nonplanar

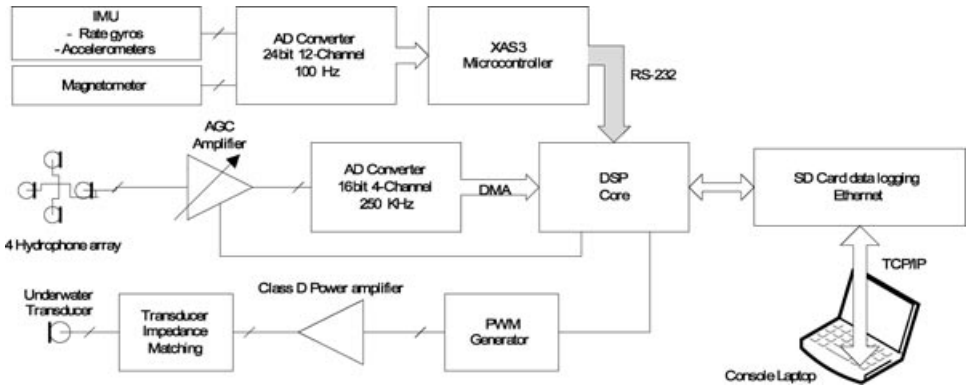

Figure 10. Integrated USBL/INS system diagram.

configuration (which allows for a three-dimensional transponder localization) and is coupled to the aluminum pressure tube using a specially designed coupling device carved from Delrin highly resistant polymer plastic. The pinger that interrogates the transponder is an ITC® 1042 and is also attached to the array coupling device.

Installed inside the system tube, a D.SignT® digital signal processor (DSP) (D.SignT, 2010) package provides the main processing power of the system that *i*) performs acoustic signal detection using high-speed fast Fourier transforms (FFTs), *ii*) generates interrogation signals to the transponder using pulse width modulation (PWM), *iii*) provides system data logging, and *iv*) includes an Ethernet interface to a console computer (which is used only for system configuration, system status checks, and data upload/download). The power is provided by a 3,700 mAh 11.1 V lithium polymer (LiPo) battery and a bank of direct-current to direct-current (DC-DC) converters, allowing for an estimated over 4 h system autonomy if used as a stand-alone system. When coupled to an underwater robotic vehicle, power can be supplied from the vehicle's own power and the Ethernet interface becomes available for data communications with the vehicle's control systems. The main system blocks are depicted in Figure 10. The processor is a Texas Instruments® C6713 floating point DSP and the acoustic signal acquisition is performed by a D.SignT® ADDA16 card which provides four 16-bit resolution synchronous acquisition channels, each with a sampling rate of 250 kHz. This acquisition card is connected to four automatic gain controlled (AGC) signal amplifiers, whose gain can either be set in automatic mode or overridden by an analogue voltage control, from a digital-to-analog converter (DAC) also available on the DSP module. The receiving amplifiers are fine-tuned to operate on the band of 20–30 kHz.

To interrogate the transponder, the DSP card generates PWM (with an update rate of 250 kHz and a resolution of 1/200 steps of PWM) through a complex programmable logic device (CPLD) that drives the transmission power amplifier and an underwater acoustic transducer. The power amplifier and acoustic transducer system are also fine-tuned to transmit maximum energy on the band of 20–30 kHz. A 16-bit card (also designed in-house) with a Phillips® XAS3 microcontroller and a bank of 12 synchronous 24-bit high-performance Sigma-Delta analog-to-digital converters (ADCs) provide the sampling capabilities of the IMU. From this ADCs bank, nine of the channels sample the triads of accelerometers and rate gyros that constitute the IMU and the magnetometers, whereas two other channels provide supply voltage and accelerometer casing temperature sampling for best performance achievement. Sampling rates of up to 150 Hz can be selected, without loss of performance. A RS-232 serial link, with a baud rate of 115,200 bps, is the interface between the DSP module and the microcontroller.

The IMU and magnetometer are pictured in Figure 11, where the triad of single-axis rate gyros can be seen on the left of the aluminum frame, and the accelerometer's triad is housed inside the black casing. This aluminum frame also supports the flux-gate magnetometer triad card above the accelerometer casing, as depicted in Figure 11. This sensor suite was previously tested and validated in other operational systems. The calibration of the IMU is also performed in-house using a high-performance inertial calibration table. The unit depicted in Figure 11(a) uses a Crossbow® CXL02TG3 triaxial accelerometer, three Silicon Sensing® CRS03 rate gyros, and the Crossbow® CXM113 triaxial flux-gate magnetometer.

At a high level, the system works as follows: the microcontroller collects data from the IMU and sends them to the DSP via the RS-232 serial link. The RS-232 interface on the DSP receives the data and stores them in memory using direct memory access (DMA) controllers without interrupting the core processor, which is doing time-critical acoustic signal processing. The DSP processes these data when possible at noncritical time-points. At prespecified instants of time (e.g., once a second), the DSP sends out a ping to the transponder and turns on the receiving subsystem to

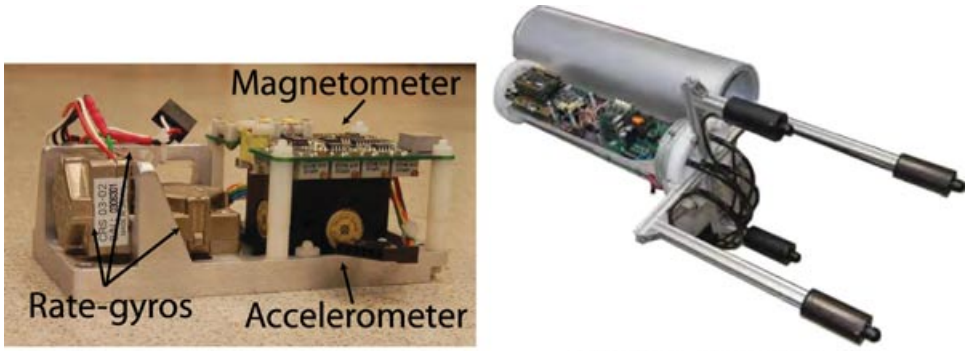

(a) Inertial measurement unit and magnetometer support frame (b) Acoustic array and core processing systems

Figure 11. Prototype system: IMU, acoustic array and core processing systems.

listen for the responses. After several pinging events and responses, and based on several factors such as vehicle maximum speed underwater sound speed, and others, the DSP is able to start closing the listening time-windows to improve multipath rejection. If responses from the transponder eventually get lost, the DSP rolls back to a fully open time search window until it gets a lock again. The prototype under development is depicted in Figure 11(b), where the acoustic array and IMU core processing systems can be seen attached to one of the covers of the pressure-housing aluminum tube.

The signal detection subsystem operates using a two-level scheme: the first, called raw-detection, is time-critical and uses fast computations on the input signal to comply with the speed at which the signal is updated at the inputs. This phase completes the processing of one predefined signal channel while storing all the data for all channels in memory. This raw-detection scheme operates using matched-filters of the expected signal based FFTs and overlap-add convolution mechanisms, as illustrated in Figure 12. Upon a correct detection of the signal in one channel, the signal is guaranteed by the detection scheme to be fully available on all channels; then, the listening subsystem is turned off and a fine-detection scheme is performed on all channels to obtain the TOA of the signal at each hydrophone.

5.2. Transponder System Overview

The transponder system is simply a subset of the previously described integrated USBL/INS system in Section 5.1. This system has to listen for ping requests sent by the USBL/INS system and respond to them with a predefined signal after a predefined interval of time. For this purpose, the transponder only requires a receiving channel and does not need the IMU and the microcontroller to interface with it.

Thus, the transponder system inherits from the previously described system the following blocks: the DSP with the acoustic acquisition card and the PWM generator, one AGC amplifier, the emission power amplifier, the battery and bank of DC-DC converters, and one acoustic transducer that serves as a receiving hydrophone and as a transmitting transducer. Additional electronics are also added for coupling the transmitting and receiving circuits to the same acoustic transducer in order to avoid the appearance of high transmission voltages at the receiving ADCs when responding to the ping requests.

5.3. Acoustic Signaling Techniques Overview

The design of any underwater acoustic ranging system requires a measurement of the time-of-flight (TOF) of a signal. As for any coherent detection problem, an accurate TOF estimate may be obtained by passing the input signal through a matched-filter whose impulse response is a time-reversed replica of the expected signal (Tolstoy, 1993). Under ideal conditions, the filter output is related to the autocorrelation function of the received signal. Acoustic signals have been used for precise underwater range measurement by TOF of acoustic waves in recent decades (Milne, 1983). Historically, due to the simplicity of the hardware involved, sinusoidal pulses were the primary choice for underwater

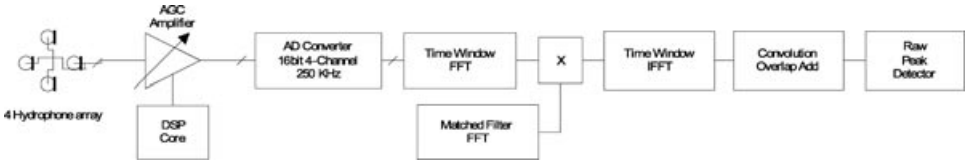

Figure 12. Raw detection scheme.

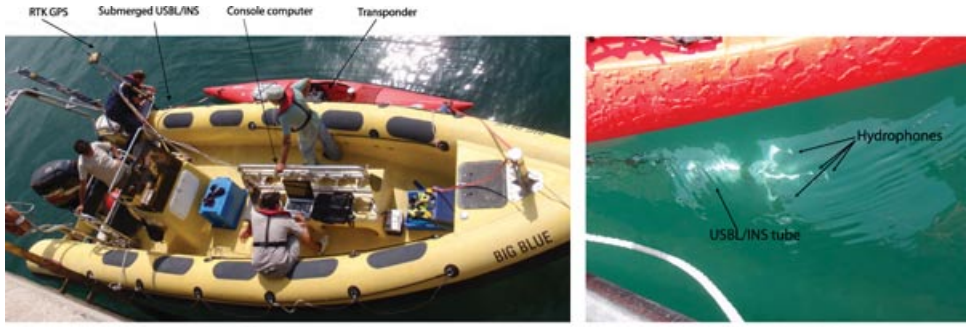

(a) Boat and transponder (b) Submerged system

Figure 13. Experimental system mounted on a support vessel—The USBL/INS system tube and acoustic array are submerged under approximately 2 m of water. The platform is allowed to swivel, attached to the end of an aluminum rod to avoid structural stress, damages, and unwanted vibrations, even though a series of cables are restricting the movement of the submerged system.

range measurements. Recent advances and the availability of low-cost, high-speed DSP hardware and software, amplifiers, and wide band acoustic transducers have allowed for the use of more advanced signaling techniques, such as chirp tone bursts and spread-spectrum signals (Austin, 1994; Bingham et al., 2007).

Specially designed spread-spectrum modulated signals have interesting autocorrelation properties (Sarwate and Pursley, 1980) allowing for a narrower output peak of the matched-filter and improving the performance of the detector. In practice, the output peak of the matched-filters spreads in time, mainly due to unequalized distortions and nonideal conditions, thus degrading the performance of such detectors. In general, spread-spectrum signals have several advantages when compared to conventional signaling for underwater range estimation: they present a better signal-to-noise ratio (SNR), robustness to ambient and jamming noise, multiuser capabilities, improved detection jitter, and the ability to better resolve multipath, which is one of the biggest problems in underwater channel acoustic propagation. These specially designed signals are typically generated using either a frequency hopping spread-spectrum sequence (FHSS) or direct spread-spectrum sequence (DSSS) codes. In the scope of the work presented herein, the attention is focused on DSSS modulated signals. Closely related work can be found in Austin (1994) and Bingham et al. (2007).

The acoustic signaling techniques employed in the experimental setup were directly inherited from the contributions presented by Morgado et al. (2011), where a novel methodology for the design and implementation of transmission pulse-shaping filters was proposed. The new design concept is based on closed-loop control strategies with preview information, and it was shown to be able to improve the detection of the transmitted signals by directly modifying the transmission pulse-shaping filters. The performance enhancement was evident from the presented simulation results and was validated using real data from experimental sea trials.

6. EXPERIMENTAL VALIDATION

Experimental trials were conducted at sea in Sesimbra, Portugal, to assess the feasibility of the tightly coupled USBL/INS system under development. In these tests, the aluminum pressure tube with the attached array was securely suspended on the side of a surface vessel, as depicted in Figure 13, at a depth of approximately 2 m, while the transponder was installed on a kayak with the transducer, also submerged approximately 2 m deep. To obtain valid evaluation datasets, both the acquisition and the transmission of the acoustic signals were synchronized with the GPS one-pulse-per-second (1-PPS) clock signal. A total of five deployments of the navigation system, labeled deployments #1, #2, #3, #4, and #5, are reported in this section. All the deployments were recorded using real-time kinematics (RTK) GPS receivers with a precision better than 4 cm.

To assess the navigation system capabilities on typical vehicle manoeuvres, the support vessel with the USBL/INS attached follows a lawn mower trajectory on deployment #1, as depicted in Figure 14(a), moving toward the transponder, which was installed on a kayak and moored to two buoys maintaining a steady position throughout the entire trajectory. Several key parameters, such as the nominal magnetic field vector and the local gravity vector, were evaluated prior to the mission using the coordinates of a reference point near the operation area. From this point forward, this reference point also serves as the origin of the north-east-down (NED) coordinates position representation on the local tangent plane (LTP) reference frame. Thus, using magnetic charts (Macmillan et al., 2004), the local magnetic field vector is given by ${}^{\{E\}}\mathbf{m} = [\,0.2645\ -0.0149\ 0.3464\,]^T$ G, which means a declination angle of

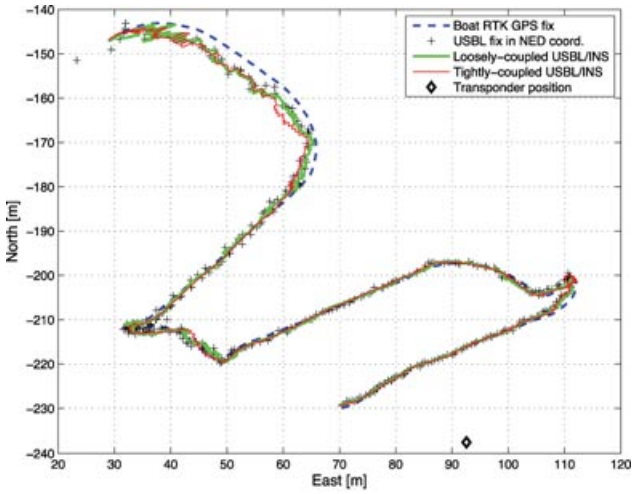

(a) North and East coordinates

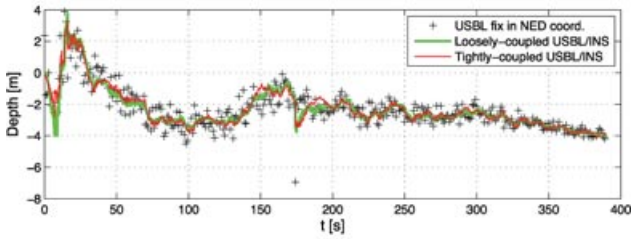

(b) Down coordinate

Figure 14. Support vessel trajectory on deployment #1 with the USBL/INS filter estimates, USBL fixes, and transponder position. The transponder position was calibrated with the onboard RTK GPS prior to the beginning of the trajectory. The loosely coupled and tightly coupled filter estimates are also plotted together with the resulting USBL position fixes in north-east-down (NED) coordinates represented on the local tangent plane (LTP) reference frame. The performance enhancement is not immediately discernible in this figure—see Figure 18(b) for a better illustration of the performance enhancement on this deployment.

approximately −3.22 deg and a dip angle of about 52.6 deg. Using local gravity charts (Imagery and Agency, 2000), the local gravity constant is given by $g = 9.8002$ m/s^2. The USBL receivers were placed on the array at the locations given by

$$
\begin{aligned}
{}^{\{C\}}\mathbf{b}_1 &= [0.1790\ -0.15\ 0]^T \text{ m},\\
{}^{\{C\}}\mathbf{b}_2 &= [0.3885\ 0\ -0.15]^T \text{ m},\\
{}^{\{C\}}\mathbf{b}_3 &= [0.1790\ 0.15\ 0]^T \text{ m},\\
{}^{\{C\}}\mathbf{b}_4 &= [0.3885\ 0\ 0.15]^T \text{ m},
\end{aligned}
$$

relative to a reference frame $\{C\}$ located on the cover of the aluminum housing cylinder. The origin of the $\{C\}$ reference frame is located 0.3 m from the body-fixed reference frame along the x axis, that is, ${}^B\mathbf{p}_C = [\,0.3\ 0\ 0\,]^T$ m. None of these quantities was actually calibrated using specific calibration procedures, but rather they were measured mechanically. The underwater sound velocity was measured at the operation depth using a sound velocity profiler (SVP) and set at a constant value of 1515 m/s.

The inertial sensor experimental noise characteristics were evaluated using benchmark datasets obtained with the platform stationary after the internal temperature of the accelerometers was stabilized. The accelerometer and rate gyro noise variances were found to be very close to those provided in each respective technical data sheet, whereas the magnetometer noise needed to be adjusted from the magnitude of 60 μG indicated on the data sheet to a more experimentally suitable 0.6 mG (evaluated with the platform stationary for several minutes before starting the trajectory). In fact, the temperature of the accelerometers is a critical factor in the stability of the overall system estimates as the accelerometer biases are known to vary with temperature. Bearing in mind the low-cost and complexity of these types of units, no steps toward temperature compensation of the accelerometers were taken whatsoever. The filter structure must tackle this issue by modeling the biases as slowly time-varying to accommodate such variations. The magnetometers were calibrated prior to the mission using a batch-processing method known as the TWOSTEP algorithm (Alonso and Shuster, 2002).

The acquired USBL data for the trajectory in deployment #1 are represented in the USBL reference frame $\{U\}$ in Figure 15. Immediately after the system start-up, acoustic outliers are evident, suggesting the need to have an efficient causal outlier detection scheme, as the EKF is highly sensitive to outliers present in the input data. Although other solutions could be devised in place of the EKF, such as outlier-robust Kalman filters (Gandhi and Mili, 2010), the solution implemented in this work was based on prefiltering the acoustic data with an explicit outlier detection causal filter prior to feeding the ranging and RDOA information to the EKF. The filter used in this work is the median absolute deviation (MAD) outlier detection and rejection filter (Menold et al., 1999), a causal filter based on the median of a running window with nine (9) acoustic samples. This filter does not change the input data nor does it introduce phase, only acting as an active valid/outlier data classifier. The behavior of the outlier classifier is shown to correctly identify the outliers present in Figure 15.

To experimentally evaluate the time-difference-of-arrival (TDOA) noise on the USBL acoustic system, the measured TDOA raw data were smoothed using a symmetrical running average window with a width equivalent to five (5) acoustic samples, and they were then compared to the actual raw data. The difference of arrival in terms of taps or samples, where one tap is equivalent to an acoustic sample time of 4 μs = (250 kHz)$^{-1}$, is presented in Figure 16. Ignoring the obvious outliers in the

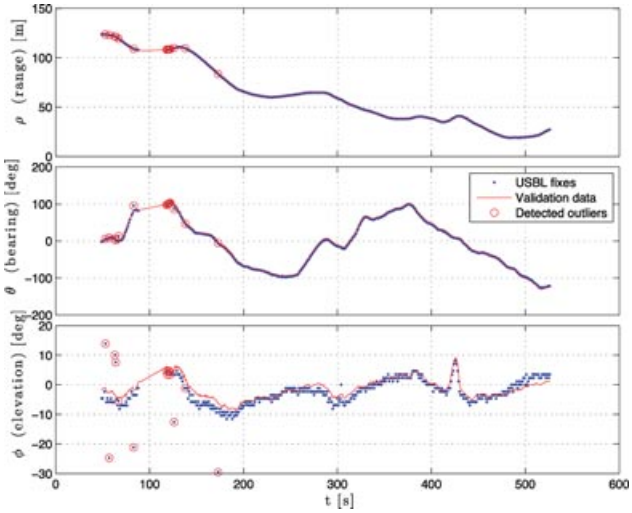

Figure 15. USBL processed position fixes on deployment #1—440 fixes represented from a total of 451 detected receptions (97.56% validated). The remaining detected acoustic receptions violated physical constraints of the receiving array such as the maximum delay taps between any two hydrophones. A total of 14 outliers (3.2%) were correctly classified as outliers. The validation data are obtained from a smoothed estimate of the IMU tilt angles and calibrated magnetometer heading, i.e., without removal of accelerometer biases, thus the validation data are biased by a tilt error from the accelerometer biases and serve only to evaluate the alignment of the sensor frames and dynamic behavior of the sensor data.

beginning of the comparison, the standard deviation between the smoothed and raw data is actually less than one tap, which was considered in the numerical simulation results presented in this work. Although not represented here, the range between the two stations was found to be less than 0.2 m during the entire trajectory.

To avoid the initial gap in acoustic data around the 100 s mark, the navigation phase is set to start at $t = 130$ s, allowing the filter to properly align and converge without acoustic data outages. The behavior of the system under USBL data outage will be discussed and analyzed next. The filters are initialized with the mean values of the GPS recorded position from the five seconds prior to the beginning of the navigation phase. The velocity estimate and all the inertial sensor bias estimates are set to zero. The filters estimates and USBL position fixes in NED coordinates in the local tangent plane (LTP) reference frame are also represented in Figure 14, where the performance enhancement is not immediately discerned. A thorough analysis is required to further assess the performance and compare both strategies experimentally. In fact, as the platform was swivelling below the supporting vessel, there were no ground truth data readily available in the LTP reference frame. To evaluate the overall performance of the navigation filters, a performance comparison will be provided using the USBL smoothed raw data as ground truth in the reference frame of the USBL by converting the estimated position in the LTP reference frame to the USBL reference frame, and also by using the integrated platform attitude estimates. The attitude estimates from both the loosely coupled and the tightly coupled filters are shown to be very similar in Figure 17.

The performance of both filters is thus evaluated in USBL coordinates, which reflects an overall assessment from both the estimated position and the attitude. This allows the results to be further compared with smoothed data from the USBL raw position fixes, which are unaffected by the platform tilt estimation errors (potentially inherited from estimation errors of the accelerometer biases). Both filter position estimates converted to the USBL reference frame are plotted in Figure 18(a). Smoothing out the raw USBL position fixes with symmetric running average filters (with a width equivalent to five acoustic samples) allows for the error comparison in Figure 18(b). The same evaluation methodology is applied to deployment #2 reported in Figure 18(d) and to deployments #3, #4, and #5 reported in Figure 19. Although the performance improvement in deployments #1 and #4 is not as clearly evidenced by the simulation results as the other deployments, the tightly coupled filter is shown to perform slightly better than the loosely coupled version. Nonetheless, the performance improvement is more evident from the comparison for deployment #2 in Figure 18(d), for deployment #3 in Figure 19(b), and for deployment #5 in Figure 19(f), and also from the overall position RMS estimation error comparison summarized in Table III. Computing the improvement level of the tightly coupled filter in the five deployments reported in Table III yields the median improvement level of approximately 15% of the tightly coupled filter against the loosely coupled version.

Ultimately, the performance of the overall system is closely related to the capabilities of such a system to estimate the inertial sensor biases. In fact, one of the ways of providing evidence of the performance enhancement of the proposed tightly coupled strategy is by showing the overall improvement of its bias estimation by forcing an outage of the USBL measurements and observing how both filters cope with the absence of data for long periods. Thus, a USBL outage was forced for 30 s, in the interval [340, 370] s, and the resulting filter output in position is plotted in Figure 20, where the tightly coupled filter is shown to diverge significantly less than the loosely coupled filter. The difference in accelerometer bias estimation between both strategies is not as easily discernible by direct comparison as when comparing the behavior during acoustic data outages. Nonetheless, the estimates of the rate gyros and accelerometer biases are shown in Figure 21, which demonstrates their slowly time varying behavior.

Improved rate gyros bias estimates are also demonstrated through an open-loop INS numerical integration

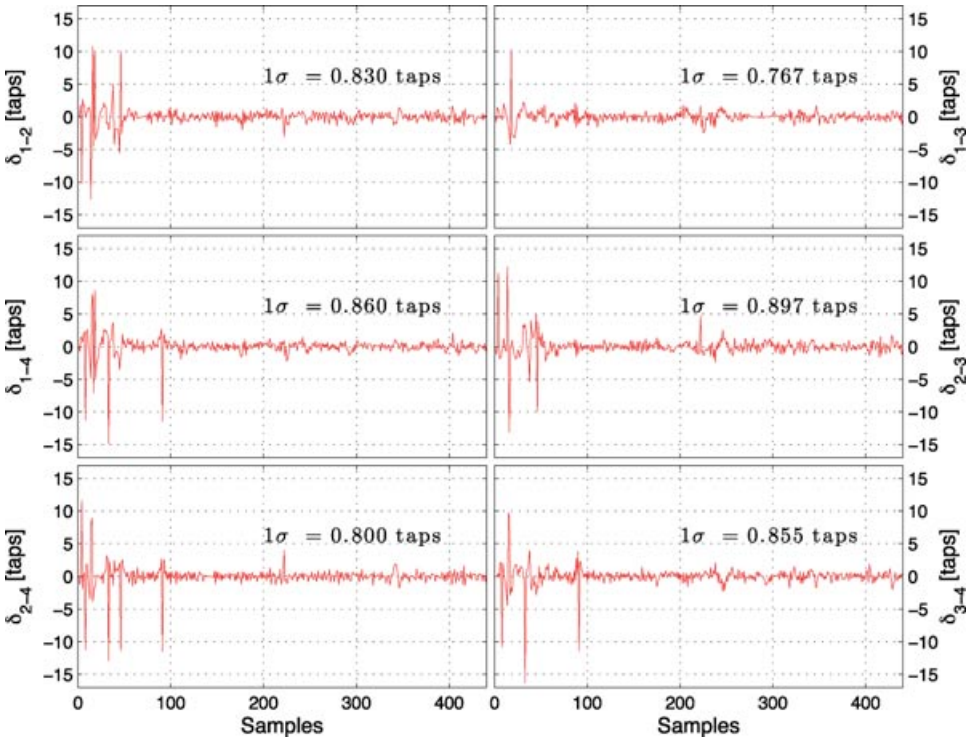

Figure 16. Experimental evaluation of USBL noise on deployment #1 in number of taps in TDOA computation—The evaluation data represent the error in the TDOA computation in number of taps (where one tap corresponds to an acoustic sample time) when comparing the raw TDOA data to a 5-s window running-average filter. The computed 1σ standard deviation for each TDOA is calculated ignoring outliers.

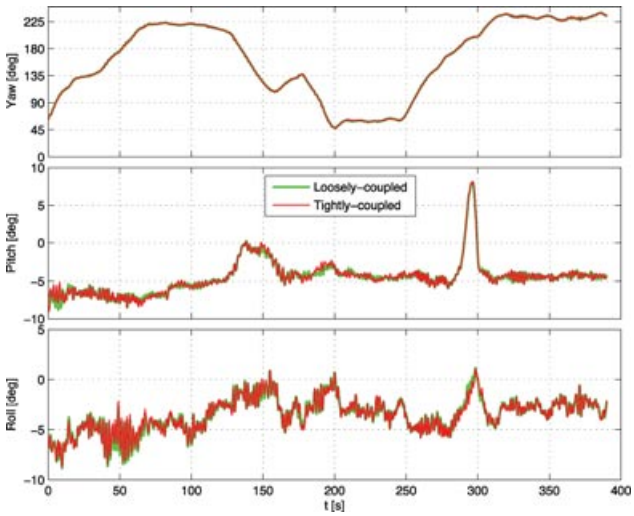

Figure 17. Estimated attitude on deployment #1—as the platform was swivelling below the support vessel, there were no ground truth data readily available for attitude evaluation purposes. Nonetheless, an overall performance comparison is performed in the sequel.

assessment of the bias-compensated rate gyros measurements in Figure 22. The estimated rate gyros biases from both strategies are used to correct the rate gyros measurements, which are then fed to the INS attitude numerical integration schemes in an open loop for approximately 6.5 min, starting at 50 s into deployment #4. These open-loop integration results are compared in Figure 22(b), revealing a smaller drift for the novel tightly coupled technique, which ultimately demonstrates improved rate gyros bias estimates and enhanced overall attitude estimation.

Another case that demonstrates enhanced performance in practice is the faster and improved convergence to the nominal trajectory from multiple initial conditions on deployment #5, reported in Figure 23. An interesting advantage of the tightly coupled filtering technique can also be found in the handling of outliers. Acoustic outliers are typically caused by incorrect detection in specific combinations of acoustic receivers, not necessarily in all possible pairs of receivers. In such situations, the tightly coupled filter has the advantage of being able to use only a subset of the TDOA measurements, as opposed to the loosely coupled solution, in which an error in a single TDOA measurement causes immediate outliers in the position fix. Such an

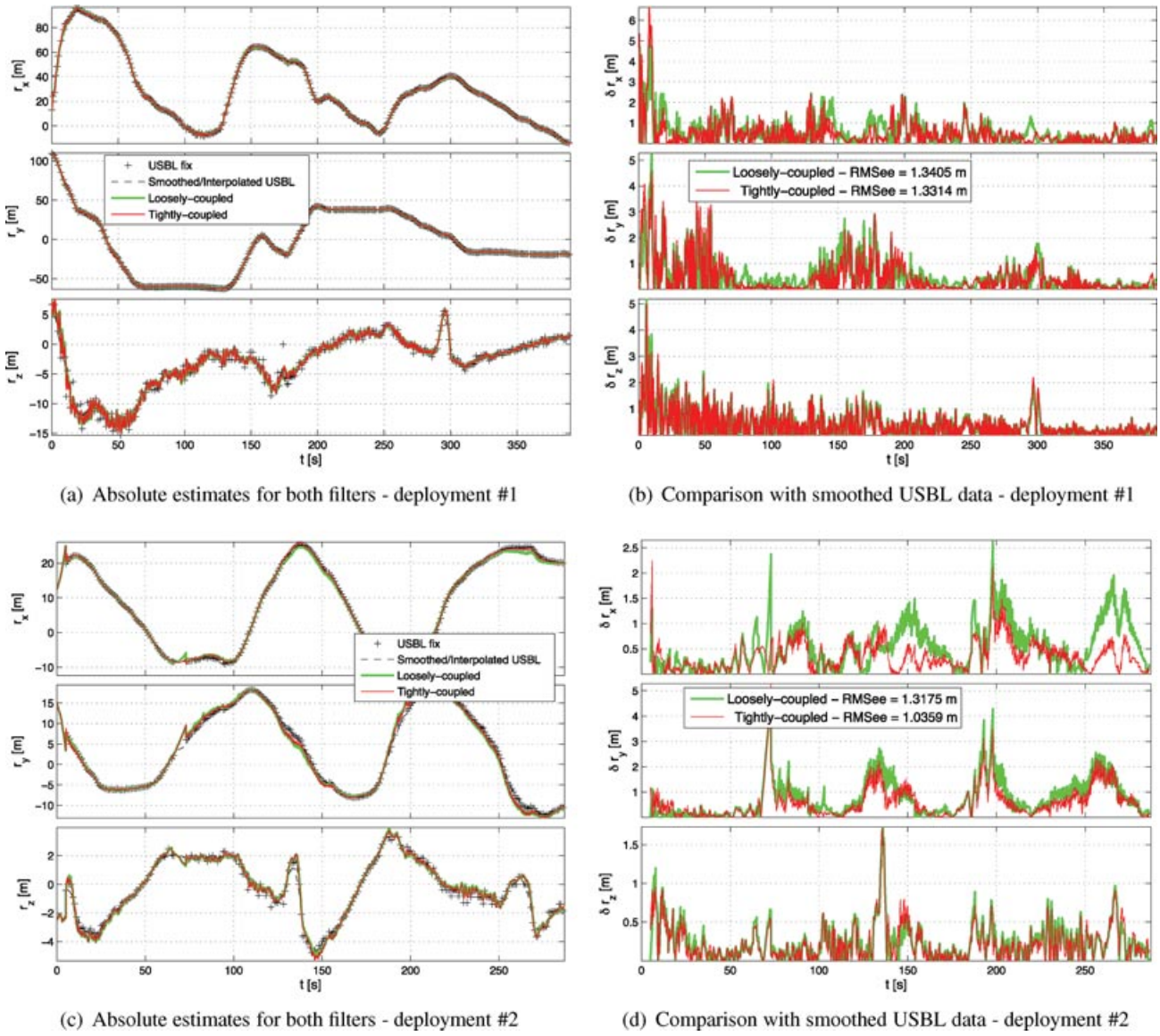

(a) Absolute estimates for both filters - deployment #1

(b) Comparison with smoothed USBL data - deployment #1

(c) Absolute estimates for both filters - deployment #2

(d) Comparison with smoothed USBL data - deployment #2

Figure 18. INS estimates on deployments #1 and #2 converted to the USBL reference frame—the position estimates of the USBL/INS system are converted to the USBL reference frame using the estimated attitude. This allows for an overall performance assessment by directly comparing the filter outputs to the acoustic positioning data. The error is obtained from comparing the INS estimates converted to the USBL reference frame, with a 5-s window running-average filter smoothed USBL trajectory.

example from deployment #3 is illustrated in Figure 24, in which the pair δ_{2-4} in the first two outliers, and pairs δ_{2-3} and δ_{3-4} in the first outlier, can still be used by the tightly coupled filter to provide corrections to the INS, whereas the loosely coupled filter is not able to use this information.

7. CONCLUSIONS

This paper presented a new USBL tightly coupled integration technique to enhance error estimation in low-cost strap-down INSs with application to underwater vehicles. In the proposed tightly coupled strategy, the acoustic array spatial information is directly exploited, resorting to the extended Kalman filter implemented in a direct feedback configuration. Classical loosely coupled techniques use the position fix of transponders in known positions of the mission area, computed from the range and bearing angles of the waves arriving at the onboard acoustic array. The planar wave approximation of the arriving acoustic signals is often employed to compute the position fix. The

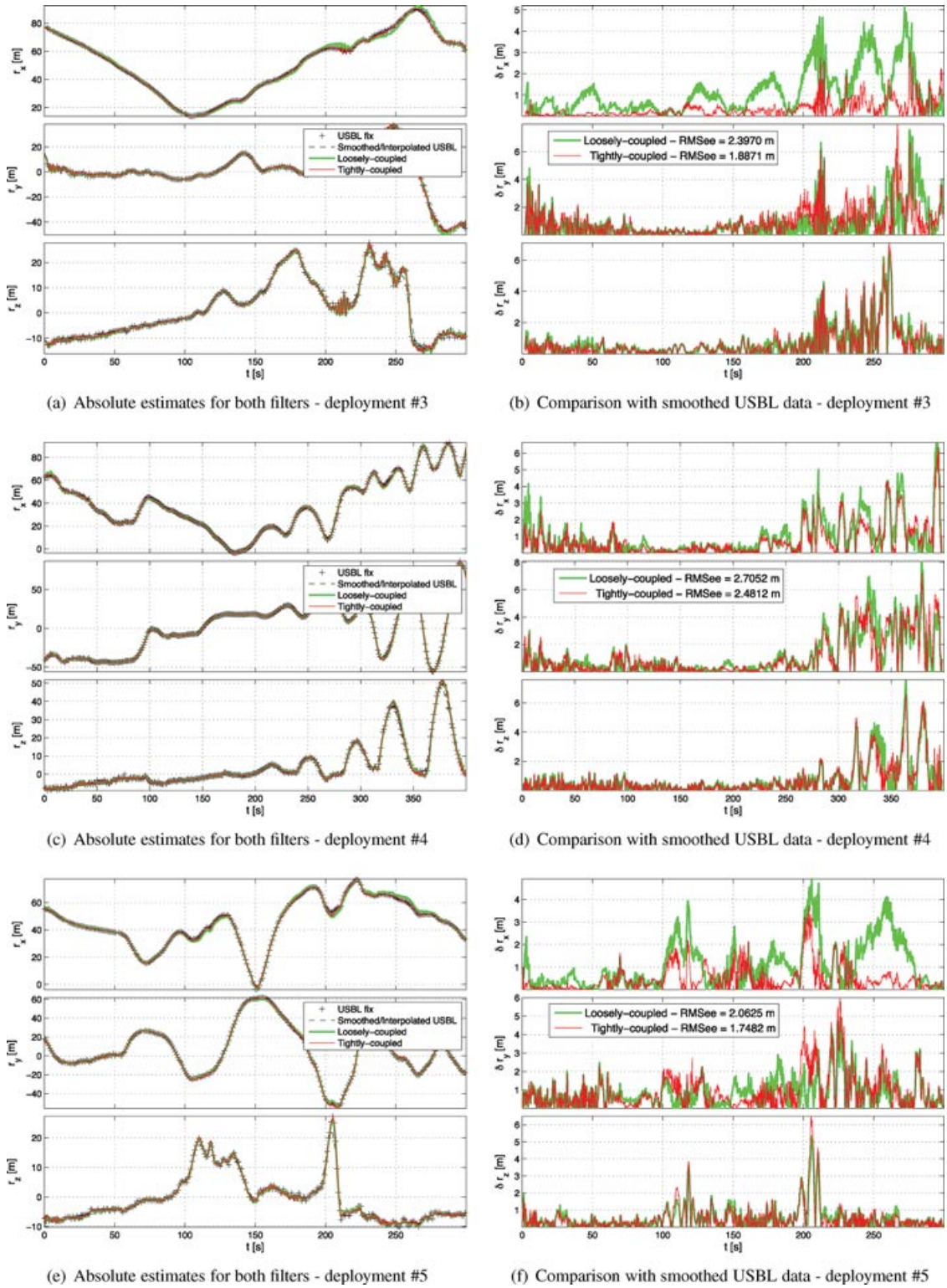

(a) Absolute estimates for both filters - deployment #3

(b) Comparison with smoothed USBL data - deployment #3

(c) Absolute estimates for both filters - deployment #4

(d) Comparison with smoothed USBL data - deployment #4

(e) Absolute estimates for both filters - deployment #5

(f) Comparison with smoothed USBL data - deployment #5

Figure 19. INS estimates on deployments #3 to #5 converted to the USBL reference frame—the position estimates of the USBL/INS system are converted to the USBL reference frame using the estimated attitude. This allows for an overall performance assessment by directly comparing the filter outputs to the acoustic positioning data.

Table III. Position RMS estimation error performance improvement overview on all deployments of the navigation filters. The median improvement level is around 15% for the tightly coupled strategy.

	Position RMS estimation error (m)				
Deployment	#1	#2	#3	#4	#5
Loosely coupled	1.3405	1.3175	2.3970	2.7052	2.0625
Tightly coupled	1.3314	1.0359	1.8871	2.4812	1.7482
Improvement level	0.7%	21.4%	21.3%	8.3%	15.3%

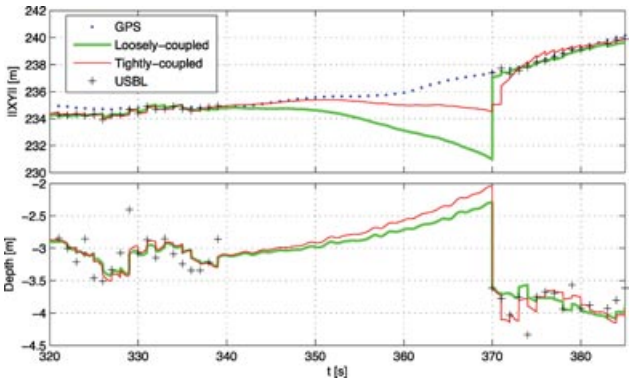

Figure 20. Inertial error evaluation during enforced USBL sensor outage on deployment #1—in order to evaluate the behavior of the system during USBL sensor outages, the USBL was shutdown for 30 s in the final straight path of the trajectory.

proposed enhancement technique makes use of the full information available from the USBL device, such as the TOA and TDOA or RDOA of the signals arriving at the different hydrophones. The physical coupling between attitude and velocity errors, evidenced in Eq. (6), also enables the use of the USBL position fixes to partially estimate attitude errors. However, as this physical attachment is invariant in the body-fixed coordinate frame, the attitude error is not fully observable solely from the rate gyros, accelerometers, and USBL measurements. Thus, an additional source of attitude information was introduced, drawn from the observations of the Earth's magnetic field, provided by an onboard magnetometer.

The overall navigation system performance was assessed in simulation using extensive Monte-Carlo simulations in which the filtering setup was exposed to different initial conditions and all the sensors to different noise sequences. The performance enhancement of this novel tightly coupled technique is evident from the numerical simulation results presented in Section 4, which compare the estimation performance of the new strategy to classical merging strategies based on loosely-coupled techniques. Moreover, the tightly coupled EKF was shown to be able to operate near the PCRLB performance lower bound, which was not attainable by the loosely coupled EKF. The proposed tightly coupled technique was further validated in an experimental setup with data acquired at sea in a total of five deployments. The inertial platform and acoustic positioning system that compose the USBL/INS system were entirely designed and built in-house, allowing the filtering architecture to have direct access to the RTT and TDOA of the acoustic waves arriving at the hydrophones on the USBL array, which is not typically provided by commercially available systems. In addition to validating the proposed technique, the experimental data obtained at sea allowed for the performance enhancement to be evidenced through real data. Although the improvement in two of the deployments was not as clear as was indicated by the simulation results and the remaining deployments, the improvement was consistent in the majority of the deployments. The median improvement level in position was demonstrated to be approximately 15%. Nonetheless, by forcing USBL sensor outages during the operation of the filters, the new tightly coupled technique was revealed to be more effective in estimating the accelerometers biases, which was reflected by the smaller position error drift during the enforced acoustic data outage. The rate gyros biases were also shown to be better estimated using the tightly coupled strategy, by comparing the attitude estimates drift error from open-loop integration of the bias-compensated

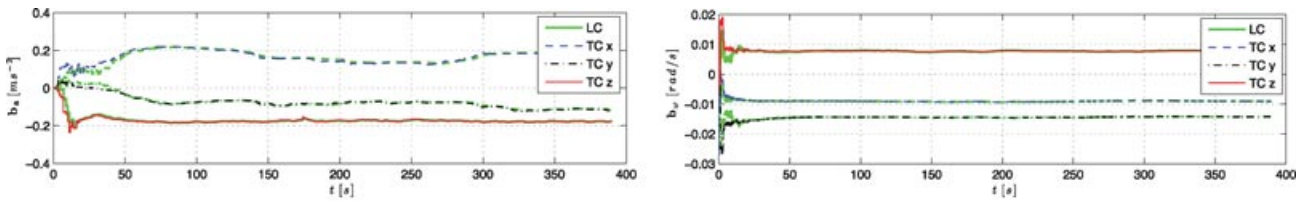

(a) Accelerometers (b) Rate gyros

Figure 21. Inertial sensor biases estimates on deployment #1—the inertial sensor estimates are shown to converge to slowly time-varying quantities. The tightly coupled (TC) estimates are overlaid over the loosely coupled (LC) biases estimates with the same line pattern and half line thickness.

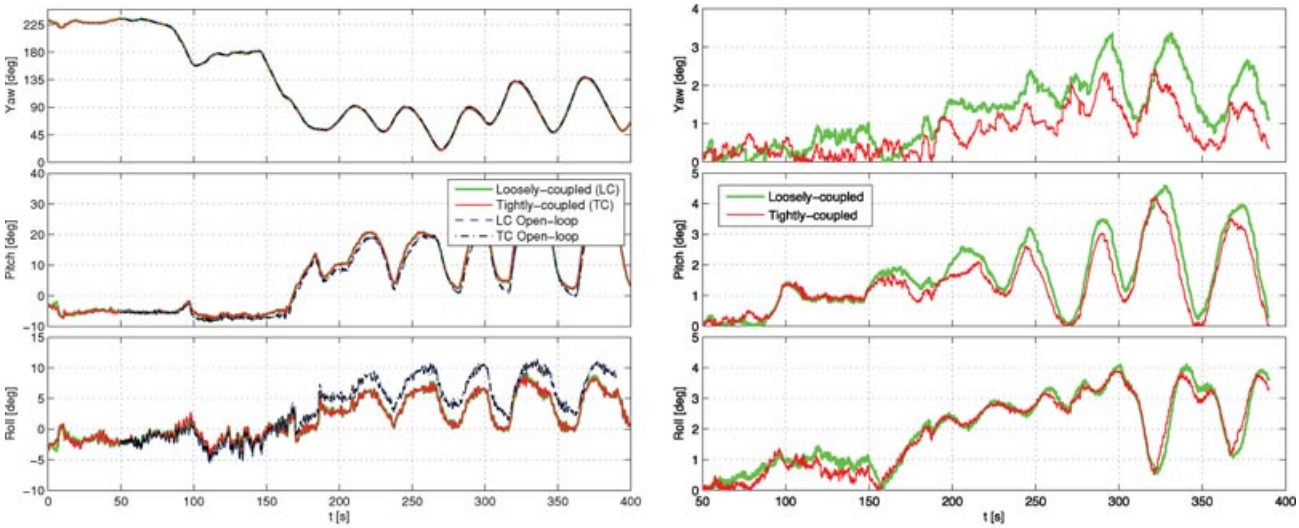

(a) Absolute estimates (b) Comparison

Figure 22. Open-loop attitude integration assessment—the bias estimates from both filtering strategies are used to correct the rate gyros measurements and numerically integrate using the INS attitude algorithms in an open loop for approximately 6.5 min, starting at 50 s into deployment #4. The smaller attitude open-loop integration drift of the tightly coupled compensated measurements demonstrates improved rate gyros bias estimates and overall enhanced attitude estimation performance.

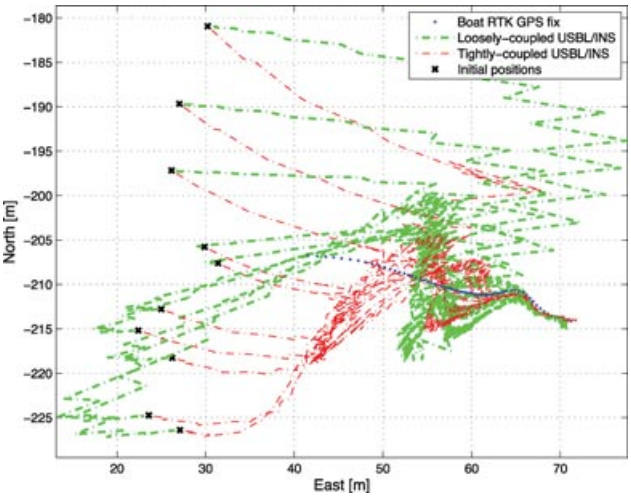

Figure 23. Convergence from multiple initial position estimates of both strategies on deployment #5 in Earth-fixed coordinates—the convergence of the tightly coupled filter is compared to the loosely coupled filter from multiple initial positions, where it can be seen that the newly proposed technique exhibits faster and improved convergence to the nominal trajectory.

angular velocity measurements. Other improvements include enhanced convergence to the nominal trajectory from multiple initial conditions, and the ability to use a subset of TDOA measurements in the tightly coupled sensor space, whereas the loosely coupled sensor space is unable to correct the INS due to detected position measurement outliers.

ACKNOWLEDGMENTS

This work was supported by FCT (ISR/IST plurianual funding) through the PIDDAC Program funds, and partially funded by the project FCT PTDC/EEA-CRO/111197/2009 - MAST/AM of the FCT and by the EU Project TRIDENT (Contract No. 248497). The work of M. Morgado was supported by a Ph.D. Student Scholarship with reference SFRH/BD/25368/2005, from the Fundação para a Ciência e a Tecnologia. The authors also gratefully acknowledge the contribution of Manuel Rufino, Bruno Cardeira, Luis Sebastião, João Botelho, Pedro Serra, André Oliveira, João Oliveira, Pedro Batista, and Tiago Gaspar throughout the development of the prototype and sea trials.

APPENDIX A: USBL POSITION FIX COMPUTATION

The USBL system computes the range and direction of the transponders using the planar approximation of the acoustic waves as in the classical approach presented in Yli-Hietanen et al. (1996).

Using the planar-wave approximation, illustrated in Figure 25, it can be written for any RDOA,

$$\rho_i - \rho_j = -(\mathbf{b}_i - \mathbf{b}_j)^T \mathbf{d}.$$

In matrix form, for all possible RDOA measurements comes

$$\mathbf{A}\mathbf{d} = -\Delta,$$

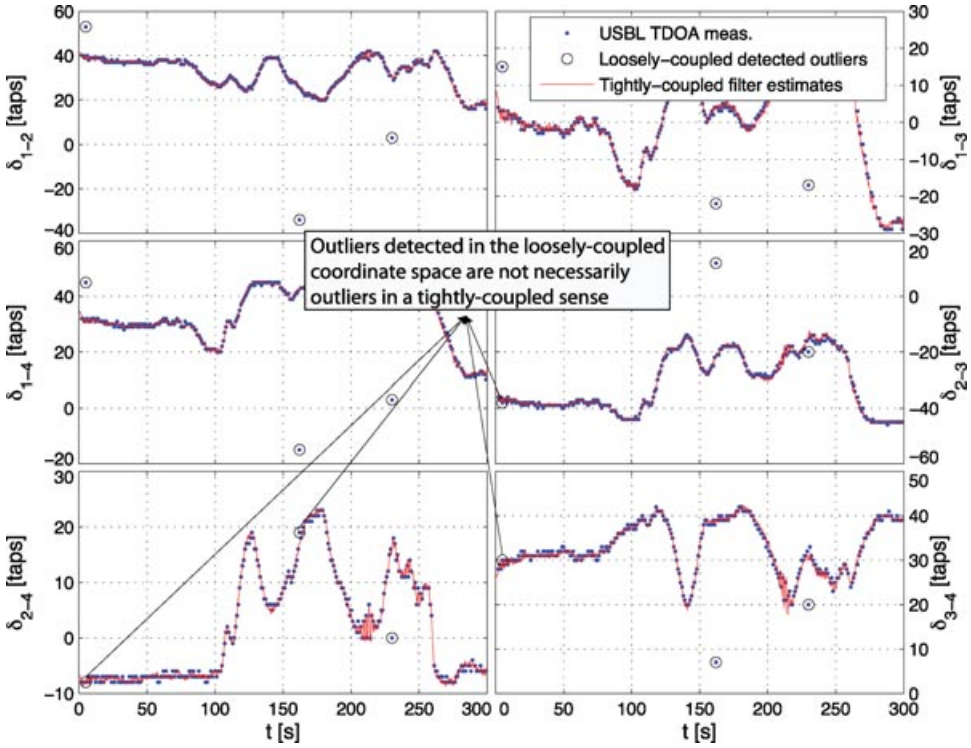

Figure 24. Measured time-difference-of-arrival (TDOA) on deployment #3—three incorrect measurements were detected by the outlier detection algorithm designed in the Cartesian sensor-space of the loosely coupled solution. These outliers are caused by incorrect detection in specific combinations of acoustic receivers, not necessarily in all possible pairs of receivers, as is the case of pair δ_{2-4} in the first two outliers, and pairs δ_{2-3} and δ_{3-4} in the first outlier. In such situations, the tightly coupled filter has the advantage of being able to use only a subset of the TDOA measurements, as opposed to the loosely coupled solution, in which an error in a single TDOA measurement causes outliers in the position fix.

where

$$\mathbf{A} = \begin{bmatrix} (\mathbf{b}_1 - \mathbf{b}_2)^T \\ (\mathbf{b}_1 - \mathbf{b}_3)^T \\ \vdots \\ (\mathbf{b}_{n_r-2} - \mathbf{b}_{n_r})^T \\ (\mathbf{b}_{n_r-1} - \mathbf{b}_{n_r})^T \end{bmatrix}, \quad \Delta = \begin{bmatrix} \rho_1 - \rho_2 \\ \rho_1 - \rho_3 \\ \vdots \\ \rho_{n_r-2} - \rho_{n_r} \\ \rho_{n_r-1} - \rho_{n_r} \end{bmatrix}.$$

To minimize the total estimation error

$$J = (\mathbf{A}\mathbf{d} + \Delta)^T \mathbf{W} (\mathbf{A}\mathbf{d} + \Delta),$$

where $\mathbf{W}$ is a weighting matrix, the unique solution for $\mathbf{d}$ is given by the well known weighted least-squares solution,

$$\mathbf{d} = -\mathbf{A}_{\mathbf{W}}^{\#} \Delta, \tag{A1}$$

where $\mathbf{A}_{\mathbf{W}}^{\#}$ is the weighted pseudoinverse matrix of $\mathbf{A}$ given by

$$\mathbf{A}_{\mathbf{W}}^{\#} = (\mathbf{A}^T \mathbf{W} \mathbf{A})^{-1} \mathbf{A}^T \mathbf{W},$$

and $\mathbf{W}$ is given by the inverse of the covariance matrix of Δ.

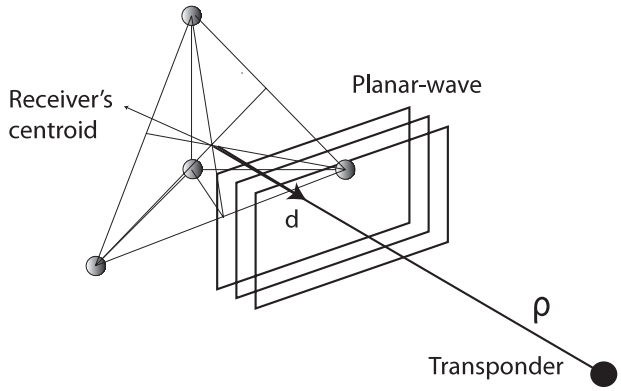

Figure 25. Planar wave approximation.

If, as assumed in this work, there is only access to independent measurements of a subset of Δ, the direction $\mathbf{d}$ is computed using only the subset of equations corresponding to those measurements. Given that the origin of the USBL frame $\{U\}$ is located at the centroid of the

receivers, the range of the transponder can be computed by averaging the measured ranges from all receivers. The relative position of a transponder expressed in $\{U\}$ is then computed by

$$\mathbf{r}_r = \rho_r \mathbf{d}_r, \tag{A2}$$

and it can be described in body-fixed coordinates by

$${}^{B}\mathbf{r}_r = \mathcal{R}^T(\mathbf{s} - \mathbf{p}) + \mathbf{n_r},$$

where $\mathbf{s}$ is the transponder's position in the Earth-fixed coordinate frame, $\mathbf{p}$ is the position of the body-fixed frame origin in the Earth-fixed frame, and $\mathbf{n_r}$ represents the relative position measurement noise, characterized by taking into account the acoustic sensor noises and the USBL positioning system (A2).

APPENDIX B: USBL POSITION FIX STOCHASTIC LINEARIZATION

The range measurements provided by the USBL system, as described in Section 3.2, are given by

$$\rho_{ir} = v_p t_{r\,i} + \eta_c + \eta_{d\,i},$$

where v_p is the underwater sound velocity, η_c represents the measurement noise induced by the common error to all receivers, and the term $\eta_{d\,i}$ represents the differential noise induced by the additional error sources and the acoustic quantization performed by the USBL system, or equivalently in matrix form,

$$\boldsymbol{\rho}_r = v_p \mathbf{t}_r + \eta_c \mathbf{1}_{n_r \times 1} + \boldsymbol{\eta}_\mathbf{d},$$

where η_c is a scalar random variable considered to be drawn from a zero mean Gaussian distribution, that is, $\eta_c \sim \mathcal{N}(0, \sigma_c^2)$, and $\boldsymbol{\eta}_\mathbf{d}$ is an $n_r \times 1$ vector random variable drawn from a zero mean Gaussian distribution with $\boldsymbol{\eta}_\mathbf{d} \sim \mathcal{N}(\mathbf{0}_{n_r \times 1}, \sigma_d^2 \mathbf{I}_{n_r})$. The random variables η_c and $\boldsymbol{\eta}_\mathbf{d}$ are also assumed to be uncorrelated, that is,

$$E\{\boldsymbol{\eta}_\mathbf{d} \eta_c\} = \mathbf{0},$$

where $E\{\cdot\}$ represents the expected value operator.

Thus, the covariance matrix for the measured ranges $\boldsymbol{\rho}_r$ is easily given by

$$E\{(\boldsymbol{\rho}_r - E\{\boldsymbol{\rho}_r\})(\boldsymbol{\rho}_r - E\{\boldsymbol{\rho}_r\})^T\} = \sigma_c^2 \mathbf{1}_{n_r \times n_r} + \sigma_d^2 \mathbf{I}_{n_r}.$$

The relationship between the RDOA observation vector $\boldsymbol{\Delta}$ and the measured distances $\boldsymbol{\rho}_r$ is established as

$$\boldsymbol{\Delta} = \mathbf{C}\boldsymbol{\rho}_r,$$

where $\mathbf{C}$ is a combination matrix that encodes the combinations between the receivers to generate the RDOA vector and is given by

$$\mathbf{C} = \begin{bmatrix} 1 & -1 & 0 & 0 & \cdots & 0 \\ 1 & 0 & -1 & 0 & \cdots & 0 \\ & & & \vdots & & \\ 0 & \cdots & 0 & 1 & 0 & -1 \\ 0 & \cdots & 0 & 0 & 1 & -1 \end{bmatrix}.$$

Taking into account the least-squares solution for the transponder direction (A1), the transponder direction covariance is given by

$$E\{(\mathbf{d} - E\{\mathbf{d}\})(\mathbf{d} - E\{\mathbf{d}\})^T\} = \mathbf{A}_\mathbf{W}^\# \mathbf{C}\left(\sigma_c^2 \mathbf{1}_{n_r \times n_r} + \sigma_d^2 \mathbf{I}_{n_r}\right)\mathbf{C}^T \mathbf{A}_\mathbf{W}^{\#\mathbf{T}}.$$

The range from the transponder to the centroid of the USBL array is computed from averaging the range measurements of all receivers, and its covariance is given by

$$E\{(\rho - E\{\rho\})^2\} = \frac{1}{n_r^2} \mathbf{1}_{1 \times n_r}\left(\sigma_c^2 \mathbf{1}_{n_r \times n_r} + \sigma_d^2 \mathbf{I}_{n_r}\right)\mathbf{1}_{1 \times n_r}^T.$$

The covariance between the measured range ρ_r and the direction $\mathbf{d}_r$ becomes

$$E\{(\rho - E\{\rho\})(\mathbf{d} - E\{\mathbf{d}\})^T\} = -\frac{1}{n_r} \mathbf{1}_{1 \times n_r}\left(\sigma_c^2 \mathbf{1}_{n_r \times n_r} + \sigma_d^2 \mathbf{I}_{n_r}\right)\mathbf{C}^T \mathbf{A}_\mathbf{W}^{\#\mathbf{T}}.$$

The position measurement (A2) can be separated into its three Cartesian components as

$$\mathbf{r}_r = \begin{bmatrix} \rho d_x & \rho d_y & \rho d_z \end{bmatrix}^T. \tag{B1}$$

Let the scalar function $g : \{\mathbb{R}^+; [0, 1]\} \to \mathbb{R}$ be given by

$$g(\rho, d_k) = \rho d_k, \quad k = \{x, y, z\},$$

which allows Eq. (B1) to be written as

$$\mathbf{r}_r = \begin{bmatrix} g(\rho, d_x) & g(\rho, d_y) & g(\rho, d_z) \end{bmatrix}^T. \tag{B2}$$

Using a Taylor series expansion of Eq. (B2) around the nominal values of $\bar{\rho}$ and $\bar{d}_k$ yields

$$g(\rho, d_k) = g(\bar{\rho}, \bar{d}_k) + \nabla g(\bar{\rho}, \bar{d}_k) \begin{bmatrix} \rho - \bar{\rho} \\ d_k - \bar{d}_k \end{bmatrix} + \frac{1}{2} \begin{bmatrix} \rho - \bar{\rho} & d_k - \bar{d}_k \end{bmatrix} \nabla^2 g(\bar{\rho}, \bar{d}_k) \begin{bmatrix} \rho - \bar{\rho} \\ d_k - \bar{d}_k \end{bmatrix} + \text{h.o.t.} \tag{B3}$$

The gradient $\nabla g(\bar{\rho}, \bar{d}_k)$ in Eq. (B3) is given by

$$\nabla g(\rho, d_k)\Big|_{\substack{\rho = \bar{\rho} \\ d_k = \bar{d}_k}} = \begin{bmatrix} \dfrac{\partial g(\rho, d_k)}{\partial \rho} & \dfrac{\partial g(\rho, d_k)}{\partial d_k} \end{bmatrix} = \begin{bmatrix} \bar{d}_k & \bar{\rho} \end{bmatrix}.$$

The second-order derivative $\nabla^2 g(\bar{\rho}, \bar{d}_k)$ is given by

$$\nabla^2 g(\rho, d_k)\Big|_{\substack{\rho=\bar{\rho} \\ d_k=\bar{d}_k}} = \begin{bmatrix} \dfrac{\partial^2 g(\rho, d_k)}{\partial^2 \rho} & \dfrac{\partial^2 g(\rho, d_k)}{\partial \rho \partial d_k} \\ \dfrac{\partial^2 g(\rho, d_k)}{\partial d_k \partial \rho} & \dfrac{\partial^2 g(\rho, d_k)}{\partial^2 d_k} \end{bmatrix} = \begin{bmatrix} 0 & 1 \\ 1 & 0 \end{bmatrix}.$$

The higher-order terms (h.o.t.) in Eq. (B3) are all null because all derivatives of $g(\bar{\rho}, \bar{d}_k)$ over the second order are also null. Thus, the expected value of $g(\rho, d_k)$ is given by (Papoulis, 1984)

$$E\{g(\rho, d_k)\} = \int_{-\infty}^{\infty} \int_{-\infty}^{\infty} g(\rho, d_k) f(\rho, d_k) \partial\rho \partial d_k, \tag{B4}$$

where $f(\rho, d_k)$ is the joint probability density function of ρ and d_k, which verifies (Papoulis, 1984)

$$\int_{-\infty}^{\infty} \int_{-\infty}^{\infty} f(\rho, d_k) \partial\rho \partial d_k = 1.$$

Combining Eqs. (B3) and (B4) yields

$$E\{g(\rho, d_k)\} = \bar{\rho}\bar{d}_k + E\{(\rho - \bar{\rho})(d_k - \bar{d}_k)\}.$$

Thus, the expected value of the transponder relative position is given by

$$E\{\mathbf{r}\} = \begin{bmatrix} E\{g(\rho, d_x)\} \\ E\{g(\rho, d_y)\} \\ E\{g(\rho, d_z)\} \end{bmatrix},$$

and its covariance can be written as

$$E\{(\mathbf{r} - E\{\mathbf{r}\})(\mathbf{r} - E\{\mathbf{r}\})^T\} = \begin{bmatrix} V_{xx} & V_{xy} & V_{xz} \\ V_{yx} & V_{yy} & V_{yz} \\ V_{zx} & V_{zy} & V_{zz} \end{bmatrix},$$

where the matrix elements V_{kj} with $k = x, y, z$ and $j = x, y, z$ are given by

$$\begin{aligned} V_{kj} &= E\{(g(\rho, d_k) - E\{g(\rho, d_k)\})\}\{(g(\rho, d_j) - E\{g(\rho, d_j)\})\} \\ &= \bar{d}_k \bar{d}_j E\{(\rho - \bar{\rho})^2\} + \bar{d}_k \bar{\rho} E\{(\rho - \bar{\rho})(d_j - \bar{d}_j)\} \\ &\quad + \bar{d}_j \bar{\rho} E\{(\rho - \bar{\rho})(d_k - \bar{d}_k)\} \\ &\quad + \bar{\rho}^2 E\{(d_k - \bar{d}_k)(d_j - \bar{d}_j)\}. \end{aligned}$$

APPENDIX C: PERFORMANCE BOUNDS

Consider the general form for the process and observation models,

$$\begin{aligned} \mathbf{x}_{k+1} &= \mathbf{f}_k(\mathbf{x}_k, \mathbf{w}_k), \\ \mathbf{z}_k &= \mathbf{h}_k(\mathbf{x}_k, \mathbf{v}_k), \end{aligned} \tag{C1}$$

where $\mathbf{x}_k$ is the system state at sample time k, $\{\mathbf{z}_k\}$ is the set of available measurements, $\{\mathbf{w}_k\}$ and $\{\mathbf{v}_k\}$ are independent white processes, and $\mathbf{f}_k$ and $\mathbf{h}_k$ are possibly nonlinear nonstationary functions.

Let $\hat{\mathbf{x}}_k$ be any estimate of the true state vector of the process given by Eqs. (C1). Since we are interested in the class of unbiased estimators for the state vector, we have the following inequality for the covariance of the estimation error:

$$\mathbf{P}_k = E\{[\hat{\mathbf{x}}_k - \mathbf{x}_k][\hat{\mathbf{x}}_k - \mathbf{x}_k]^T\} \geq \mathbf{J}_k^{-1},$$

where $\mathbf{J}_k$ is the posterior Fisher information matrix (FIM) defined as

$$\mathbf{J}_k = E\big\{ - \nabla_{\mathbf{x}_k} \nabla_{\mathbf{x}_k}^T \log p(\mathbf{x}_k, \mathbf{z}_k)\big\},$$

where $p(\mathbf{x}_k, \mathbf{z}_k)$ is the joint probability density function of the state vector and observations throughout the full extent of the trajectory of the underlying dynamical system. Tichavskỳ et al. (1998) showed that the FIM $\mathbf{J}_k$ can be efficiently computed using the following recursion:

$$\mathbf{J}_{k+1} = \mathbf{D}_k^{22} - \mathbf{D}_k^{21} \big(\mathbf{J}_k + \mathbf{D}_k^{11}\big)^{-1} \mathbf{D}_k^{12},$$

where

$$\begin{aligned} \mathbf{D}_k^{11} &= E_{p(\mathbf{x}_{k+1}|\mathbf{z}_{k+1})} \left\{ -\nabla_{\mathbf{x}_k} \nabla_{\mathbf{x}_k}^T \log p(\mathbf{x}_{k+1}|\mathbf{x}_k) \right\}, \\ \mathbf{D}_k^{12} &= E_{p(\mathbf{x}_{k+1}|\mathbf{z}_{k+1})} \left\{ -\nabla_{\mathbf{x}_k} \nabla_{\mathbf{x}_{k+1}}^T \log p(\mathbf{x}_{k+1}|\mathbf{x}_k) \right\} = \left[\mathbf{D}_k^{21} \right]^T, \\ \mathbf{D}_k^{22} &= E_{p(\mathbf{x}_{k+1}|\mathbf{z}_{k+1})} \left\{ -\nabla_{\mathbf{x}_{k+1}} \nabla_{\mathbf{x}_{k+1}}^T \log p(\mathbf{x}_{k+1}|\mathbf{x}_k) \right\} \\ &\quad + E_{p(\mathbf{x}_{k+1}|\mathbf{z}_{k+1})} \left\{ -\nabla_{\mathbf{x}_{k+1}} \nabla_{\mathbf{x}_{k+1}}^T \log p(\mathbf{z}_{k+1}|\mathbf{x}_{k+1}) \right\}, \end{aligned} \tag{C2}$$

and the recursion is initialized with

$$\mathbf{J}_0 = E\left\{ -\nabla_{\mathbf{x}_0} \nabla_{\mathbf{x}_0}^T \log p(\mathbf{x}_0) \right\}.$$

To compute the terms in Eqs. (C2), the expected value operator $E_{p(\mathbf{x}_{k+1}|\mathbf{z}_{k+1})}\{\cdots\}$ needs to be evaluated. The computational complexity of these expectations depends entirely on the structure of the underlying process and observation models, and involves solving integral terms that, in general, do not have closed-form solutions in the particular case of the estimators presented herein. As suggested in Šimandl et al. (2001), the terms can be estimated using Monte-Carlo simulations by replacing the expected values with the sample mean of the realizations, e.g., the term $\hat{\mathbf{D}}_k^{11}$ in Eqs. (C2) is computed as

$$\hat{\mathbf{D}}_k^{11} = \frac{1}{M} \sum_{j=1}^{M} -\nabla_{\mathbf{x}_k} \nabla_{\mathbf{x}_k}^T \log p(\mathbf{x}_{k+1}|\mathbf{x}_k)\,\big|_{\mathbf{x}_k = \mathbf{x}_k(j)},$$

where $\{\mathbf{x}_k(j)\}_{k=0}^N$ is the jth realization of the state trajectory, $j = 1, 2, \ldots, M$, and M is the number of Monte-Carlo realizations.

As expected, as M increases, the quality of the Monte-Carlo estimates improves, however there is no rule of thumb on selecting an M that guarantees that the estimates will be satisfactory. One possible rule is to

try several values for M and test if the new bound with M_2 realizations has changed significantly compared to the bound with $M_1 < M_2$ realizations.

In the scope of the work presented herein, we restrict the PCRLB evaluation to the discrete-time AWGN case for which the process and observation models are given by

$$\begin{aligned}\mathbf{x}_{k+1} &= \mathbf{f}_k(\mathbf{x}_k) + \mathbf{w}_k,\\ \mathbf{z}_k &= \mathbf{h}_k(\mathbf{x}_k) + \mathbf{v}_k,\end{aligned}$$

where $\mathbf{x}_k$ now represents the discretized errors of the navigation systems at sample time k, $\{\mathbf{w}_k\}$ is the process equivalent AWGN, $\{\mathbf{v}_k\}$ is the measurement equivalent AWGN, $\{\mathbf{z}_k\}$ is the set of available measurements that are related to the state vector by the nonlinear nonstationary observation function $\mathbf{h}_k$, and $\mathbf{f}_k$ models the discretized navigation system error model.

In this framework, the logarithmic terms of the PCRLB recursion can be written as

$$\begin{aligned}\log p(\mathbf{x}_{k+1}, \mathbf{x}_k) &= c_1 - \frac{1}{2}[\mathbf{x}_{k+1} - \mathbf{f}_k(\mathbf{x}_k)]^T \mathbf{Q}_k^{-1}\\ &\quad \times [\mathbf{x}_{k+1} - \mathbf{f}_k(\mathbf{x}_k)],\\ \log p(\mathbf{z}_{k+1}, \mathbf{x}_{k+1}) &= c_2 - \frac{1}{2}[\mathbf{z}_{k+1} - \mathbf{h}_{k+1}(\mathbf{x}_{k+1})]^T \mathbf{R}_{k+1}^{-1}\\ &\quad \times [\mathbf{z}_{k+1} - \mathbf{h}_{k+1}(\mathbf{x}_{k+1})],\end{aligned}$$

where c_1 and c_2 are constants, $\mathbf{Q}_k$ is the discrete equivalent process AWGN covariance matrix, and $\mathbf{R}_k$ is the discrete equivalent observation AWGN covariance matrix.

Thus, it can be easily derived for the terms (C2) that

$$\begin{aligned}\mathbf{D}_k^{11} &= E\left\{\mathbf{F}_k^T(\mathbf{x}_k)\mathbf{Q}_k^{-1}\mathbf{F}_k(\mathbf{x}_k)\right\},\\ \mathbf{D}_k^{12} &= -E\left\{\mathbf{F}_k^T(\mathbf{x}_k)\right\}\mathbf{Q}_k^{-1},\\ \mathbf{D}_k^{22} &= \mathbf{Q}_k^{-1} + E\left\{\mathbf{H}_{k+1}^T(\mathbf{x}_{k+1})\mathbf{R}_{k+1}^{-1}\mathbf{H}_{k+1}(\mathbf{x}_{k+1})\right\},\end{aligned}$$

where

$$\begin{aligned}\mathbf{F}_k(\mathbf{x}_k) &= \left[\nabla_{\mathbf{x}_k}\mathbf{f}_k^T\right]^T,\\ \mathbf{H}_{k+1}(\mathbf{x}_{k+1}) &= \left[\nabla_{\mathbf{x}_{k+1}}\mathbf{h}_{k+1}^T\right]^T\end{aligned}$$

are the Jacobian matrices of $\mathbf{f}_k$ and $\mathbf{h}_{k+1}$, respectively, evaluated at their true values.

APPENDIX D: INTERNAL INS DETAILS

For highly manoeuvrable vehicles, the INS numerical integration must properly address the angular, velocity, and position high-frequency motions, referred to as coning, sculling, and scrolling, respectively, to avoid the buildup of estimation errors. The INS multirate approach, based on the work detailed in Savage (1998a; 1998b), computes the dynamic angular rate/acceleration effects using high-speed, low-order algorithms, whose output is periodically fed to a moderate-speed algorithm that computes attitude/velocity resorting to exact, closed-form equations. Applications within the scope of this work are characterized by confined mission scenarios and limited operational time, allowing for a simplification of the frame set to Earth and body frames and the use of an invariant gravity model without loss of precision.

The inputs provided to the inertial algorithms are the integrated inertial sensor output increments

$$\boldsymbol{\upsilon}(\tau) = \int_{t_{k-1}}^{\tau} \mathbf{a}_r\, dt, \qquad \boldsymbol{\alpha}(\tau) = \int_{t_{k-1}}^{\tau} \boldsymbol{\omega}_r\, dt,$$

where $\boldsymbol{\omega}_r$ represents the rate gyro triad readings and $\mathbf{a}_r$ represents the accelerometer readings, also known as the measured body specific force,

$$\mathbf{a}_r \triangleq {}^B\mathbf{a}_{SF} = {}^B\dot{\mathbf{v}} + \boldsymbol{\omega} \times {}^B\mathbf{v} - {}^B\mathbf{g},$$

where ${}^B\mathbf{g}$ is the nominal local gravity vector in body coordinates ${}^B\mathbf{g} = \mathcal{R}^T {}^E\mathbf{g}$, and ${}^E\mathbf{g}$ is the locally constant gravity vector in Earth-fixed coordinates.

The inertial sensor readings are corrupted by zero mean white noise $\mathbf{n}$ and random-walk bias, $\dot{\mathbf{b}} = \mathbf{n}_b$, yielding

$$\begin{aligned}\mathbf{a}_r &= {}^B\dot{\mathbf{v}} + \boldsymbol{\omega} \times {}^B\mathbf{v} - {}^B\mathbf{g} - \delta\hat{\mathbf{b}}_a + \mathbf{n}_a,\\ \boldsymbol{\omega}_r &= \boldsymbol{\omega} - \delta\hat{\mathbf{b}}_\omega + \mathbf{n}_\omega,\end{aligned}$$

where $\delta\hat{\mathbf{b}} = \hat{\mathbf{b}} - \mathbf{b}$ denotes bias compensation error, $\mathbf{b}$ is the nominal bias, $\hat{\mathbf{b}}$ is the estimated bias, and the subscripts a and ω identify accelerometer and rate gyro quantities, respectively.

The attitude moderate-speed algorithm (Savage, 1998b) computes body attitude in DCM form,

$${}^{B_{k-1}}_{B_k}\mathbf{R}(\boldsymbol{\lambda}_k) = \mathbf{I}_3 + \frac{\sin\|\boldsymbol{\lambda}_k\|}{\|\boldsymbol{\lambda}_k\|}(\boldsymbol{\lambda}_k)_\times + \frac{1-\cos\|\boldsymbol{\lambda}_k\|}{\|\boldsymbol{\lambda}_k\|^2}(\boldsymbol{\lambda}_k)_\times^2, \quad \text{(D1)}$$

where the operator $\|\cdot\|$ is the usual l_2-norm for vectors such that $\|x\| = (x^T x)^{\frac{1}{2}}$, $\{B_k\}$ is the body frame at time k, and ${}^{B_{k-1}}_{B_k}\mathbf{R}(\boldsymbol{\lambda}_k)$ is the rotation matrix from $\{B_k\}$ to $\{B_{k-1}\}$ coordinate frames, parametrized by the rotation vector $\boldsymbol{\lambda}_k$. The rotation vector updates are based on the Bortz equation (Bortz, 1971), and are formulated as

$$\boldsymbol{\lambda}_k = \boldsymbol{\alpha}_k + \boldsymbol{\beta}_k$$

in order to denote angular integration and coning attitude terms $\boldsymbol{\alpha}_k$ and $\boldsymbol{\beta}_k$, respectively. The attitude high-speed algorithm computes $\boldsymbol{\beta}_k$ as a summation of the high-frequency angular rate vector changes using simple, recursive computations (Savage, 1998a), providing high-accuracy results.

Using the equivalence between strap-down attitude and velocity/position algorithms (Roscoe, 2001), the same multirate approach is applied (Savage, 1998b) to compute exact velocity updates at moderate speed,

$$\mathbf{v}_k = \mathbf{v}_{k-1} + {}^E_{B_{k-1}}\mathbf{R}\,\Delta^{B_{k-1}}\mathbf{v}_{\mathrm{SF\,k}} + \Delta\mathbf{v}_{\mathrm{G/Cor\,k}},$$

where $\Delta^{B_{k-1}}\mathbf{v}_{\mathrm{SF\,k}}$ is the velocity increment related to the specific force, and $\Delta\mathbf{v}_{\mathrm{G/Cor\,k}}$ represents the velocity increment due to gravity and the Coriolis effect (Savage, 1998b). The term $\Delta^{B_{k-1}}\mathbf{v}_{\mathrm{SF\,k}}$ also accounts for high-speed velocity rotation and high-frequency dynamic variations due to angular rate vector rotation, yielding

$$\Delta^{B_{k-1}}\mathbf{v}_{\mathrm{SF\,k}} = \boldsymbol{\upsilon}_k + \Delta\mathbf{v}_{\mathrm{rot\,k}} + \Delta\mathbf{v}_{\mathrm{scul\,k}},$$

where $\Delta\mathbf{v}_{\mathrm{rot\,k}}$ and $\Delta\mathbf{v}_{\mathrm{scul\,k}}$ are the rotation and sculling velocity increments, respectively, computed by the high-frequency algorithms. Interestingly enough, a standard low-power consumption DSP-based hardware architecture is sufficient for running the INS algorithms using maximal computational accuracy at high execution rates. This allows using maximal precision so that the computational accuracy of the INS output is only diminished by the inertial sensor noise and biases effects.

REFERENCES

Alonso, R., & Shuster, M. (2002). Complete linear attitude-independent magnetometer calibration. Journal of the Astronautical Sciences, 50(4), 477–490.

Austin, T. (1994). The application of spread spectrum signaling techniques to underwater acoustic navigation. In Proceedings of the 1994 Symposium on Autonomous Underwater Vehicle Technology, 1994, AUV '94.

Bar-Shalom, Y., Li, X., Kirubarajan, T., & Wiley, J. (2001). Estimation with applications to tracking and navigation. Wiley Online Library.

Bingham, B., Blair, B., & Mindell, D. (2007). On the design of direct sequence spread-spectrum signaling for range estimation. In Proceedings of the OCEANS '07 MTS/IEEE, Vancouver, Canada.

Bortz, J. (1971). A new mathematical formulation for strapdown inertial navigation. IEEE Transactions on Aerospace and Electronic Systems, 7(1), 61–66.

Bowen, A., Yoerger, D., Taylor, C., McCabe, R., Howland, J., Gomez-Ibanez, D., Kinsey, J., Heintz, M., McDonald, G., Peters, D., et al. (2009). The Nereus hybrid underwater robotic vehicle. Underwater Technology: The International Journal of the Society for Underwater, 28(3), 79–89.

Britting, K. (1971). Inertial navigation systems analysis. John Wiley & Sons, Inc.

Brown, R. G., & Hwang, P. Y. C. (1997). Introduction to random signals and applied Kalman filtering. 3rd ed. John Wiley & Sons.

Crassidis, J. (2006). Sigma-point Kalman filtering for integrated gps and inertial navigation. IEEE Transactions on Aerospace and Electronic Systems, 42(2), 750–756.

D.SignT (2010). D.Module.C6713 technical data sheet. http://www.dsignt.de/download/tdd6713.pdf. Rev. 1.4.

Eustice, R., Singh, H., & Whitcomb, L. (2011). Synchronous-clock, one-way-travel-time acoustic navigation for underwater vehicles. Journal of Field Robotics, 28(1), 121–136.

Gandhi, M., & Mili, L. (2010). Robust Kalman filter based on a generalized maximum-likelihood-type estimator. IEEE Transactions on Signal Processing, 58(5), 2509–2520.

Gelb, A. (1974). Applied optimal estimation. Cambridge, MA: MIT Press.

Goshen-Meskin, D., & Bar-Itzhack, I. (1992). Observability analysis of piece-wise constant systems - part I: Theory. IEEE Transactions on Aerospace and Electronic Systems, 28(4), 1056–1067.

Grewal, M., Weill, L., Andrews, A., & Wiley, J. (2007). Global positioning systems, inertial navigation, and integration. Wiley Online Library.

Imagery, N., & Agency, M. (2000). World geodetic system 1984—its definition and relationships with local geodetic systems. Technical report, Department of Defense. TR8350.2 Amendment 1.

Jaffré, F., Austin, T., Allen, B., Stokey, R., & Von Alt, C. (2005). Ultra short baseline acoustic receiver/processor. In Proceedings of the OCEANS '05 MTS/IEEE, vol. 2, pp. 1382–1385, Washington, D.C.

Jalving, B., Gade, K., Hagen, O., & Vestgard, K. (2003). A toolbox of aiding techniques for the HUGIN AUV integrated inertial navigation system. In Proceedings of the OCEANS '03 MTS/IEEE, San Diego, CA.

Kinsey, J., Eustice, R., & Whitcomb, L. (2006). A survey of underwater vehicle navigation: Recent advances and new challenges. In Proceedings of the 7th Conference on Manoeuvring and Control of Marine Craft (MCMC2006), Lisbon, Portugal. IFAC.

Kinsey, J. C., & Whitcomb, L. L. (2004). Preliminary field experience with the DVLNAV integrated navigation system for oceanographic submersibles. Control Engineering Practice, 12(12), 1541–1548. Invited paper.

Knight, D. (1997). Rapid development of tightly-coupled GPS/INS systems. IEEE Aerospace and Electronic Systems Magazine, 12(2), 14–18.

Koifman, M., & Bar-Itzhack, I. (1999). Inertial navigation system aided by aircraft dynamics. IEEE Transactions on Control Systems Technology, 7(4), 487–493.

Lee, P., Jeon, B., Kim, S., Choi, H., Lee, C., Aoki, T., & Hyakudome, T. (2004). An integrated navigation system for autonomous underwater vehicles with two range sonars, inertial sensors and Doppler velocity log. In Proceedings of the OCEANS '04 MTS/IEEE, vol. 3, pp. 1586–1593, Kobe, Japan.

Lurton, X., & Millard, N. (1994). The feasibility of a very-long baseline acoustic positioning system for AUVs. In Proceedings of the OCEANS '04 IEEE Europe, vol. 3, pp. 403–408, Brest, France.

Macmillan, S., McLean, S., & Maus, S. (2004). The US/UK world magnetic model for 2005-2010. Technical report, NOAA.

Menold, P., Pearson, R., & Allgower, F. (1999). Online outlier detection and removal. In Proceedings of the 7th International Conference on Control and Automation MED99, pp. 1110–1134, Haifa, Israel.

Miller, P., Farrell, J., Zhao, Y., & Djapic, V. (2010). Autonomous underwater vehicle navigation. IEEE Journal of Oceanic Engineering, 35(3), 663–678.

Milne, P. (1983). Underwater acoustic positioning systems. Gulf Pub. Co.

Morgado, M., Oliveira, P., & Silvestre, C. (2010). Design and experimental evaluation of an integrated USBL/INS system for AUVs. In Proceedings of the 2010 IEEE International Conference on Robotics and Automation (ICRA), pp. 4264–4269, Anchorage, AK.

Morgado, M., Oliveira, P., & Silvestre, C. (2011). A closed-loop design methodology for underwater transducers pulse-shaping. In Proceedings of the 2011 IEEE International Conference on Mechatronics and Automation (ICMA), pp. 2014–2019, Beijing, China.

Morgado, M., Oliveira, P., Silvestre, C., & Vasconcelos, J. (2006). USBL/INS tightly-coupled integration technique for underwater vehicles. In Proceedings of the 9th IEEE International Conference on Information Fusion, Florence, Italy.

Napolitano, F., Cretollier, F., & Pelletier, H. (2005). GAPS, combined USBL + INS + GPS tracking system for fast deployable and high accuracy multiple target positioning. In Proceedings of the OCEANS '05 IEEE Europe, Brest, France.

Papoulis, A. (1984). Probability, Random Variables, and Stochastic Processes. McGraw-Hill, second edition.

Pascoal, A., Oliveira, P., & Silvestre, C., et al. (2000). Robotic ocean vehicles for marine science applications: The European ASIMOV Project. In Proceedings of the OCEANS '00 MTS/IEEE, Rhode Island.

Roscoe, K. (2001). Equivalency between strapdown inertial navigation coning and sculling integrals/Algorithms. AIAA Journal of Guidance, Control, and Dynamics, 24(2), 201–205.

Rugh, W. (1996). Linear system theory. 2nd ed. Prentice-Hall.

Sanz, P., Ridao, P., Oliver, G., Melchiorri, C., Casalino, G., Silvestre, C., Petillot, Y., & Turetta, A. (2010). TRIDENT: A framework for autonomous underwater intervention missions with dexterous manipulation capabilities. In Proceedings of the 7th Symposium on Intelligent Autonomous Vehicles IAV-2010. IFAC.

Sarwate, D., & Pursley, M. (1980). Cross-correlation properties of pseudorandom and related sequences. Proceedings of the IEEE, 68(5), 593–619.

Savage, P. (1998a). Strapdown inertial navigation integration algorithm design part 1: Attitude algorithms. AIAA Journal of Guidance, Control, and Dynamics, 21(1), 19–28.

Savage, P. (1998b). Strapdown inertial navigation integration algorithm design part 2: Velocity and position algorithms. AIAA Journal of Guidance, Control, and Dynamics, 21(2), 208–221.

Šimandl, M., Královec, J., & Tichavskỳ, P. (2001). Filtering, predictive, and smoothing Cramér-Rao bounds for discrete-time nonlinear dynamic systems. Automatica, 37(11), 1703–1716.

Smith, S., & Kronen, D. (1997). Experimental results of an inexpensive short baseline acoustic positioning system for AUV navigation. In Proceedings of the OCEANS '97 MTS/IEEE, vol. 1, pp. 714–720, Halifax, Nova Scotia, Canada.

Sukkarieh, S., Nebot, E., & Durrant-Whyte, H. (1999). A high integrity IMU/GPS navigation loop for autonomous land vehicle applications. IEEE Transactions on Robotics and Automation, 15(3), 572–578.

Tichavskỳ, P., Muravchik, C. H., & Nehorai, A. (1998). Posterior Cramér-Rao bounds for discrete-time nonlinear filtering. IEEE Transactions on Signal Processing, 46(5), 1386–1396.

Tolstoy, A. (1993). Matched field processing for underwater acoustics. River Edge, NJ: World Scientific.

Van Trees, H. L. (1966). Bounds on the accuracy attainable in the estimation of continuous random processes. IEEE Transactions on Information Theory, 12, 298–305.

Van Trees, H. L. (1968). Detection, estimation, and modulation theory. Part 1. Detection, estimation, and linear modulation theory. New York: Wiley.

Van Trees, H. L., & Bell, L. K. (2007). Bayesian bounds for parameter estimation and nonlinear filtering/tracking. 1st ed. John Wiley & Sons–IEEE Press.

Vasconcelos, J. F., Silvestre, C., & Oliveira, P. (2011). INS/GPS aided by frequency contents of vector observations with application to autonomous surface crafts. Journal of Oceanic Engineering, 36(2), 347–363.

Vickery, K. (1998). Acoustic positioning systems. New concepts—The future. In Proceedings of the 1998 Workshop on Autonomous Underwater Vehicles, AUV'98, Cambridge, MA.

Whitcomb, L. L. (2000). Underwater robotics: Out of the research laboratory and into the field. In Robotics and Automation, 2000. Proceedings, IEEE International Conference on ICRA'00, vol. 1, pp. 709–716.

Yi, Y., & Grejner-Brzezinska, D. (2006). Tightly-coupled GPS/INS integration using unscented Kalman filter and particle filter. In Proceedings of the 19th International Technical Meeting of the Satellite Division of The Institute of Navigation (ION GNSS), pp. 2182–2191, Fort Worth, TX.

Yli-Hietanen, J., Kalliojarvi, K., & Astola, J. (1996). Low-complexity angle of arrival estimation of wideband signals using small arrays. In Proceedings of the 8th IEEE Signal Processing Workshop on Statistical Signal and Array Processing.

Yun, X., Bachmann, E., McGhee, R., Whalen, R., Roberts, R., Knapp, R., Healey, A., & Zyda, M. (1999). Testing and evaluation of an integrated gps/ins system for small auv navigation. IEEE Journal of Oceanic Engineering, 24(3), 396–404.

Zhong, Z., Meng, H., & Wang, X. (2010). A comparison of posterior Cramér-Rao bounds for point and extended target tracking. IEEE Signal Processing Letters, 17(10), 819–822.